Oda Mohus and Anna Eikebrokk

Simulations of Characteristic Sand Behavior by DEM

Master's thesis

NTNU
Norwegian University of Science and Technology
Faculty of Engineering
Department of Civil and Environmental Engineering

NTNU

Norwegian University of
Science and Technology

Oda Mohus and Anna Eikebrokk

Simulations of Characteristic Sand Behavior by DEM

NTNU
Norwegian University of
Science and Technology

Preface

This master's thesis is written during the Spring semester of 2021 as a part of the MSc in Civil and Environmental Engineering at the Norwegian University of Science and Technology (NTNU, Trondheim). It has been carried out as a collaboration between Oda Mohus and Anna Eikebrokk, both master students in Geotechnical Engineering at NTNU. The thesis was proposed by the Norwegian Geotechnical Institute (NGI), and has been carried out in collaboration with them.

Trondheim, 2021-06-09

Oda Mohus   Anna Eikebrokk

Acknowledgment

Summary and Conclusions

The discrete element method is proposed as an important tool in the quest of understanding the fundamental behavior of granular materials. LS-DEM is a discrete element model that, by level set functions, accurately incorporates the true grain shapes in its formulation. By using a numerical model, several limitations associated with conventional laboratory testing can be eliminated. An essential part of soil characterization is to achieve several different stress paths from an identical state. However, such experiments have shown to be extremely difficult to conduct in the lab, due to limitations associated with physical sample preparation and the influence of boundary conditions. This could easily be done with LS-DEM simulations. In addition, the simulation results can be used to investigate quantities like fabric and particle rotations, which are difficult to measure in the lab, and have proven to be important for describing the overall granular behavior.

This paper presents how LS-DEM simulations can be used to calibrate the input parameters of the advanced constitutive material model, SANISAND. The simulations have been performed on Hostun sand, characterized by angular grains with low sphericity. Special focus has been set on defining the critical state line, which is currently challenging to establish from conventional laboratory testing.

SANISAND input parameters have been calibrated using Python and PLAXIS Soil Test. It was observed that all analyses reached a well defined critical state, and a location of the critical state line is proposed. However, the critical void ratio was expected to be more pressure dependent than what was observed for initial pressures $p = 10 - 500\ kPa$. The bounding surface parameter is considered well defined, whereas the results needed to calibrate the phase transformation surface were scattered, resulting in uncertainty related to the slope of this. The kinematic hardening parameters, calibrated using trial and error, yield adequate average fits between LS-DEM analyses and the SANISAND response. However, the analyses run in this thesis are not sufficient for defining them uniquely. Determining these parameters is therefore proposed as an objective for a future study. The calibrated dilatancy parameter is considered relatively certain as its fit to the LS-DEM simulations appears accurate.

To investigate the effect of incorporating realistic grain shapes in the DEM formulation, a selection of the simulations were run with spherical grains. The calibrated critical state line for Hostun sand was then compared with the corresponding critical state line for the analyses run with spherical grains. The simulations performed and investigated in this study shows that the sample consisting of true grain shapes reaches a higher critical stress ratio and void ratio than the sample with spherical grains.

Several preliminary limitations regarding the LS-DEM analyses in this study have been discussed.

Jumps in the average stresses at the boundaries were detected, indicating the occurrence of numerical instabilities in the analyses. These fluctuations can presumably be limited by reducing the applied time step. Moreover, it needs to be highlighted that the computational costs running LS-DEM constitutes a significant drawback of the method.

Finally, with calibrated input parameters, SANISAND response and LS-DEM results correspond, also for independently run numerical analyses. However, it is necessary to perform a proper validation to ensure this correspondence. Regardless, despite its limitations, LS-DEM is still considered a promising tool to understand the nature behind characteristic behavior of granular material.

Sammendrag

For å utbedre kunnskapen om granulære materialer og deres oppførsel kan diskret elementmetode være et viktig hjelpemiddel. LS-DEM er en variant av diskret elementmetode, men skiller seg fra den tradisjonelle typen ved at nøyaktig kornform inkluderes i koden. Bruk av slike numeriske modeller kan til en viss grad redusere omfanget av nødvendig laboratorietesting, samt de begrensninger disse assosieres med. Videre kan LS-DEM måle rotasjon og geometrisk konfigurasjon av enkelte partikler. Dette er egenskaper som er vanskelige å undersøke i lab, dog betydningsfulle for oppførselen til granulære materialer.

I denne oppgaven har resultater fra LS-DEM simuleringer blitt brukt som utgangspunkt for å kalibrere SANISAND-modellen. Simuleringene er utført med prøver av Hostun sand, som består av angulære og ikke-sfæriske korn. Det har spesielt blitt lagt vekt på definere en unik "critical state line", da dette foreløpig er utfordrende å gjøre med eksperimentelle resultater.

SANISAND modellparametere er kalibrert ved hjelp av Pythonskript og PLAXIS Soil Test. Alle analysene nådde samme kritiske spenningsforhold. Videre nådde alle et vel definert kritisk poretall, utifra hvilke en "critical state line" ble kalibrert. Verdien av "bounding surface" parameteren er vurdert til å være nokså nøyaktig. Datapunktene nødvendige i kalibreringen av "phase transformation" parameteren var spredt, og det knyttes dermed usikkerhet til denne verdien. "Kinematic hardening" parameterne, kalibrert ved prøve-og-feile metoden, gir SANISAND respons som passer nokså godt med LS-DEM resultatene. Men, stor usikkerhet er knyttet til disse verdiene, noe det anbefales å undersøke videre. Videre vurderes dilatansparameteren å være veldefinert, dette fordi SANISAND korresponderer med LS-DEM resultatene for deviatorisk tøyning mot volumetrisk tøyning.

Alt i alt gjengir SANISAND modellen oppførselen som er observert ved LS-DEM relativt nøyaktig. Dette underbygger både at SANISAND kan gjengi sandoppførsel under monotonisk belastning, men også at LS-DEM kan simulere karakteristisk oppførsel av friksjonsjordarter.

Ved å erstatte de realistiske kornformene i LS-DEM med sfæriske korn, ble det undersøkt hvorvidt kornformen påvirker resultatene. "Critical state" parametere for Hostun sand ble i den sammenheng sammenliknet med tilsvarende parametere kalibrert fra analysene med sfæriske korn. Denne sammenligningen viser at analysene der kornform er inkludert når høyere kritisk spenningsforhold og poretall enn analysene med sfæriske korn gjør.

Flere svakheter ved LS-DEM er belyst. Det er observert hopp i gjennomsnittsspenningene, noe som indikerer numeriske problemer i analysene. Disse variasjonene kan sannsynligvis begrenses ved å redusere tidssteget brukt i koden. I tillegg understrekes det at en betydelig mengde datakraft er nødvendig

for å kjøre LS-DEM analysene.

Med de kalibrerte modellparameterne korresponderer den oppførselen SANISAND forutsier med LS-DEM resultatene, også for uavhengige analyser. Det understrekes dog at å utføre en skikkelig validering av resultatene er nødvendig. Uansett har LS-DEM, tross sine begrensninger, fortsatt potensiale for å kunne bidra til å utvikle kunnskapen om granulære materialer.

Contents

List of Figures

List of Tables

List of Acronyms

Caltech California Institute of Technology

CD Consolidated Drained test

CU Consolidated Undrained test

CS Critical State

CSL Critical State Line

CSSM Critical State Soil Mechanics

DEM Discrete Element Method

LCC Limiting Compression Curve

LS Level Set

LS-DEM Level Set Discrete Element Method

ML Machine Learning

NGI Norwegian Geotechnical Institute

NTNU Norwegian University of Science and Technology

ODE Ordinary Differential Equation

OWT Offshore Wind Turbines

PBC Periodic Boundary Conditions

SANISAND Simple ANIsotropic SAND

UU Unconsolidated Undrained test

List of symbols

ENGLISH

Symbol	Explanation	Unit
A_d	Dilatancy parameter	$[-]$
c	Input scalar for triaxial extension	$[-]$
c_h	Kinematic hardening parameter	$[-]$
c_z	Rate of evolution of z	$[-]$
D	Dilatancy	$[-]$
D	Dimension of system	$[-]$
D_r	Relative density	$[-]$
d	Dilatancy parameter	$[-]$
$\overline{d}_{eq}$	Average equivalent grain diameter	$[m]$
d_n	Normal deflection	$[m]$
E	Elastic modulus	$[Pa]$
e	Void ratio	$[-]$
e_0	Void ratio at p_c=0	$[-]$
e_c	Critical void ratio	$[-]$
e_{max}	Void ratio in the soils loosest state	$[-]$
e_{min}	Void ratio in the soils densest state	$[-]$
F	Yield surface in stress space	$[Pa]$
G	Elastic shear modulus	$[Pa]$
G_0	Elastic shear stiffness constant	$[-]$
G_s	Specific gravity of soil particles	$[-]$
H	Plastic hardening modulus	$[-]$
h_0	Kinematic hardening parameters	$[-]$
K	Elastic bulk modulus	$[Pa]$
K_0	Elastic bulk stiffness constant	$[-]$
k_n	Normal stiffness in grain-to-grain contact	$[N/m]$
k_s	Shear stiffness in grain-to-grain contact	$[N/m]$
L	Plastic loading index	$[-]$
M	Critical stress ratio	$[-]$

m	SANISAND input parameter	$[-]$
m_s	Mass of solids	$[kg]$
n	Porosity	$[\%]$
n	Number of grains	$[\%]$
n^b	Bounding surface constant	$[-]$
n^d	Dilatancy surface constant	$[-]$
p	Mean stress	$[Pa]$
p_0	Mean stress at yield surface cap	$[Pa]$
p_{atm}	Atmospheric pressure	$[Pa]$
p_c	Mean stress at critical state	$[Pa]$
p_r	SANISAND LCC parameter	$[Pa]$
Q	Potential surface	$[Pa]$
q	Deviatoric stress	$[Pa]$
q_c	Critical deviatoric stress	$[Pa]$
q_f	Failure load	$[Pa]$
T	Natural period	$[s]$
Δt	Time step	$[s]$
$\Delta t_{critical}$	Critical time step	$[s]$
u	Pore pressure	$[Pa]$
V	Total volume	$[m^3]$
V_s	Volume of soilds	$[m^3]$
V_p	Volume of pores	$[m^3]$
v	Specific volume	$[-]$
v_c	Critical specific volume	$[-]$
X	SANISAND LCC parameter	$[-]$
z	Fabric-dilatancy internal parameter	$[-]$

GREEK

Symbol	Explanation	Unit
α	Back stress ratio	$[-]$
α_c	Back stress ratio in compression	$[-]$
α^b	Bounding surface	$[-]$
α^c	Back stress ratio at critical state	$[-]$
α^d	Phase transformation surface	$[-]$
Γ	Critical state parameter	$[-]$
γ	Specific weight	$[N/m^3]$
γ	Shear strain	$[-]$
γ^e	Elastic shear strain	$[-]$

$\varepsilon_1, \varepsilon_2, \varepsilon_3$	Principal strain	$[-]$
$\dot{\varepsilon}_1, \dot{\varepsilon}_2, \dot{\varepsilon}_3$	Principal strain rates	$[-]$
ε_p	Volumetric strain	$[-]$
ε_q	Deviatoric strain	$[-]$
ε^e	Elastic strain	$[-]$
ε^p	Plastic strain	$[-]$
η	Stress ratio	$[-]$
θ	SANISAND LCC parameter	$[-]$
κ	Stiffness level of particles	$[-]$
λ	Critical state parameter	$[-]$
ν	Poisson's ratio	$[-]$
ξ	Critical state parameter	$[-]$
ρ_c	SANISAND LCC parameter	$[-]$
ρ_s	Density of soilds	$[kg/m^3]$
ρ_w	Density of distilled water	$[kg/m^3]$
σ	(Total) stress	$[Pa]$
σ^p	Plastifying stress	$[Pa]$
$\sigma_1, \sigma_2, \sigma_3$	Principal stress	$[Pa]$
τ	Shear stress	$[Pa]$
ψ	Dilatancy angle	$[-]$
ψ	State parameter	$[-]$

Chapter 1

Introduction

1.1 Background

In order to meet the EU's goal of climate neutrality by 2050, we have to undergo a green transition, in which the consumption of oil and natural gases needs to be phased out (Geden and Schenuit, 2019). Such a green shift can be fueled by utilizing the vast potential of our sea basins in terms of establishing offshore wind turbine (OWT) farms.

Various man made structures, like offshore wind turbines, buildings and dams, are to a great extent founded on granular soils. Yet, their behavior still remains challenging to predict. Extensive efforts have been made to develop constitutive models that describe the behavior of granular materials. This has resulted in the multiple material models existing today.

Even though sand consists of individual particles, models have, for a long time, regarded sand at the macroscopic scale as a continuum. The first of these being the Mohr-Coulomb criterion, that defines a failure line solely based on the principal effective stresses, friction angle and cohesion. Since then, the continuum models have been developed, and now there exist several complex models that capture many physical phenomena of sand behavior.

Critical state soil mechanics (Schofield and Wroth, 1968) is a framework commonly used when studying soil behavior, which generally captures the stress-strain response well for a soil subjected to monotonic loading. However, this framework alone does not perform well when considering cyclic loading. Bounding Surface Plasticity theory (Dafalias, 1986) proposes a smooth transition from elastic to elasto-plastic response, where plastic strains occur both for stress states within and on the bounding surface. The family of SANISAND models (Dafalias and Manzari, 2004; Taiebat and Dafalias, 2008; Petalas et al., 2019) are elasto-plastic constitutive material models that combine the frameworks of critical state soil mechanics and bounding surface plasticity. This is done with the intention of describing the response of sand subjected to both monotonic and cyclic loading in a simple and understandable way. The model is able to replicate the response of soils subjected to monotonic loading with a high degree of accuracy. Despite extensive efforts, the model is still not able to accurately predict the cyclic behavior of granular soils (Jostad et al., 2020). This, however, is a field of on-going research (Petalas et al., 2019; Liu et al., 2018).

Such advanced material models require a unique set of input parameters, and the calibration of these

has proven to be challenging. The challenges can likely be attributed to the limitations and uncertainties of conventional laboratory testing. For the calibration procedure, several tests are necessary. To avoid sample variation, these tests should be run from the same initial fabric, which is very difficult to guarantee in the lab. Moreover, different localization patterns may develop for different stress paths, which affects the measured macroscopic response on the boundaries, making the results not directly comparable. In addition, it is difficult to reach the required strain level to uniquely define the critical state line parameters in experimental tests.

The challenges of current soil characterization methods make the design process of OWT fields unnecessarily expensive. An OWT farm may involve the construction of hundreds of turbines spread across several square kilometers of seabed. That requires soil characterization of huge areas, unlike the limited investigation area associated with the establishment of oil and gas platforms. Extracting samples and investigating the location of every OWT is practically impossible. Consequently new methods for soil characterization are necessary.

It may be possible to acquire a better replication of soil behavior by improving our understanding on how single grains interact, and incorporate this in existing material models. Recent advances in both computational power and experimental technology have made it possible to model sand as individual grains. This is done by the Discrete Element Method (DEM) (Cundall and Strack, 1979). Based on particle overlap and amount of relative shear motion, interparticle forces can be computed. With this numerical tool, simulations of loading paths challenging, or even impossible, to conduct experimentally, is feasible. In addition, important properties like the initial fabric of a sample can directly be taken as input. Further, the evolution of fabric can easily be extracted from the simulation results, as the exact position and rotation of each particle at any time is known.

Traditional DEM uses simple geometrical shapes like spheres, ellipsoids or clusters of these to describe the grain shape. This is considered a limitation since grain shape is shown to be of high importance to the mechanical behavior of soils (J. Yang and Luo, 2015). A completely realistic replication of angular grains can not be obtained this way. This gives motivation to the development of a method where the true shapes of the grains are incorporated.

Improvements in level set imaging (LS-Imaging) (Vlahinić et al., 2014), have made it possible to incorporate shape in the DEM-formulation. LS-imaging characterizes granular assemblies from XRCT-images into mathematical representations of individual particles. These are implemented in a relatively new variant of DEM, called level set discrete element method (LS-DEM) (Kawamoto et al., 2016). The incorporation of true grain shapes makes LS-DEM simulation results directly comparable to real sand behavior.

Supplementing traditional laboratory testing with LS-DEM simulations may contribute in overcoming the limitations and uncertainties associated with experimental testing today. Thereby, it may reduce uncertainty in the characterization of materials, and thus improve the workflow for foundation design of all structures founded on or off sand. Further, the economic benefits that comes along will facilitate for improved geotechnical engineering, including the construction of OWT farms, such that the potential of our sea basins may be exploited to fuel the green shift.

What Remains to be Done?

A set of SANISAND input parameters is yet to be calibrated with results from LS-DEM simulations. By limiting the shortcomings associated with traditional laboratory testing, a more reliable parameter set may be calibrated with DEM simulations. This requires a reliable model, which LS-DEM has proven to be (Kawamoto et al., 2018).

An evaluation of the importance of realistic grain shape representations may be obtained by simulating the exact same conditions for true granular soil and a close to identical sample consisting of only spherical grains.

Research Questions

This master's thesis focuses on simulating triaxial tests on specimens of Hostun sand with LS-DEM, and subsequent interpretation of the test results in order to evaluate the functionality of LS-DEM. The problem formulations are stated as follows:

- Can LS-DEM be used to establish a unique set of input parameters to the constitutive material model SANISAND for a given sand?

- To what extent will the shape of the grains affect the critical state line?

1.2 Objectives

The aim of this thesis is to study characteristic sand behavior with DEM, and further incorporation of this behavior in constitutive material models for sand. The main objectives are:

- Use LS-DEM to calibrate a unique set of input parameters for SANISAND.

- Evaluate whether grain shape affects critical state line.

1.3 Scope

This thesis concentrates on the SANISAND continuum material model. Further, due to simplicity, only drained triaxial compression is considered. Therefore, all stresses are considered effective. Plastic deformation due to crushing of grains will not be considered, neither will the phenomenon of liquefaction.

The numerical simulations are performed on Hostun sand. This sand is chosen due to its poor grading, with angular and non-spherical grains. Hostun sand has grains with particularly challenging shapes, and is therefore prone to showcase the ability of LS-DEM to simulate particles of arbitrary shape (Kawamoto et al., 2018). The analyses have been run with a cubic sample of a consistent size. A limited selection of initial void ratios and compression pressures are used. All samples are isotropically compressed. During the dynamic analyses, an explicit time integration scheme is used, and global damping is implemented.

1.4   Approach

A literature review is carried out to increase the understanding of the general features of sand behavior together with existing constitutive material models. SANISAND is investigated in particular, in terms of the input parameters necessary to describe the sand, and its theoretical ability to describe general sand behavior. Further, the discrete element method (DEM) with focus on LS-DEM has been reviewed.

The triaxial test simulations are run with LS-DEM on sand samples with 16^3 grains. Samples with initial void ratios of 0.6, 0.65, 0.8 and 1.0 are all isotropically compressed to different pressures, and then sheared.

The LS-DEM results are used in order to calibrate the SANISAND model by the use of Python plots and PLAXIS SoilTest. Firstly, the elastic stiffness parameters, G_0 and K_0, and the CSL parameters, α_c, e_{c0}, λ_c and ξ are fixed. Further, the bounding surface and dilatancy surface constants, n^b and n^d, are calibrated, before the determination of the kinematic hardening parameters, h_0 and c_h, and the dilatancy parameter, A_d.

1.5   Structure of the Report

The chapters remaining of this report are structured as follows:

Chapter 2 gives a brief review of basic definitions in granular soil theory. It further describes the basic concepts of triaxial testing, before it introduces the SANISAND continuum material model as well as the theories SANISAND is based on.

Chapter 3 presents the discrete element method (DEM), and introduces the level set variant of DEM (LS-DEM).

Chapter 4 presents the implementation of LS-DEM and describes the procedure for running the simulations.

Chapter 5 describes the calibration procedure as well as the obtained SANISAND input parameters from the LS-DEM simulation results.

Chapter 6 investigates to what extent grain shape affects the critical state line, by running analyses with spherical grains.

Chapter 7 discusses different strengths and weaknesses of our findings.

Chapter 8 gives a summary and final conclusions of the work that has been carried out. Recommendations for further work are given.

Chapter 2

Theory

2.1 Granular Soils

A granular soil is defined as a collection of particles, that can vary in both size and shape, visible to the naked eye. As opposed to microscopic particles, particles in a granular soil are big enough for it to be necessary to distinguish between their surface and their volume (Duran, 2000). Hence, volume is not sufficient to describe a grain, the shape is also of significant importance. The general behavior of a granular soil is complex as it can behave both like a solid and as a liquid. A granular material can be able to support static shear load and thereby have solid-like properties, but it can also flow in a dense state and in that way behave like a liquid.

Grain Size Distribution

The composition of a granular soil is decisive for the soil's strength properties, as well as for the deforming behavior of the material (J. Yang and Luo, 2015). The grain composition may vary a lot. When considering sand, the particle size range between 0.001 mm and 1000 mm.

Grain Shape

Two parameters are often used to describe shape; sphericity and roundness. Sphericity captures the volume and general shape of the grain (as deviation from a sphere), while roundness is given by the surface curvature at lower local scale, or the sharpness of its corners (Kawamoto et al., 2018). A grain with low roundness is characterized as angular.

Overall regularity was introduced as a shape index by (J. Yang & Luo, 2015), with the purpose of providing a collective characterization of grain shape. It is defined as the average of aspect ratio, convexity and sphericity, as illustrated in Figure 2.1.

Fabric

The fabric of a soil refers to the spatial and geometrical configuration of the sand grains (Fu and Dafalias, 2011). In other words, a complete description of the state of a soil. In micromechanics, fabric is typi-
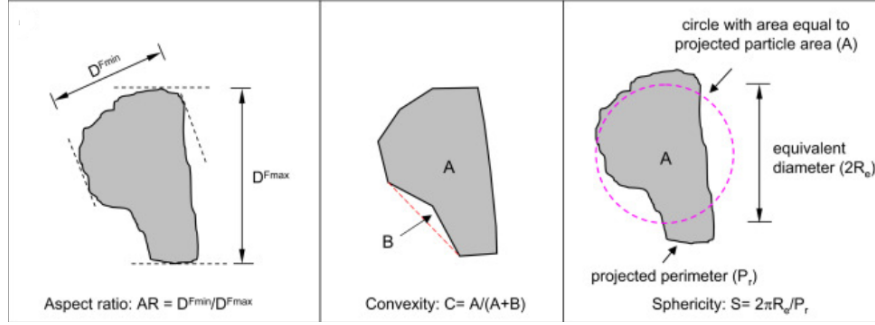
Figure 2.1: Definition of sphericity, aspect ratio and convexity (from J. Yang and Luo, 2015).

cally quantified by tensors. The most commonly used categories of such tensors are particle orientation-based, contact normal-based and void-based fabric tensors (Wang et al., 2017). In order to describe the fabric accurately, the grains exact location, orientation and shape needs to be known.

Grains tend to align their longest side parallel to the bedding and normal to gravity. Therefore, granular soils normally have different properties in different directions, i.e. they are anisotropic. This should also be assessed when considering the fabric of a soil. Figure 2.2 shows how two different initial fabrics are obtained by the use of two different packing methods.
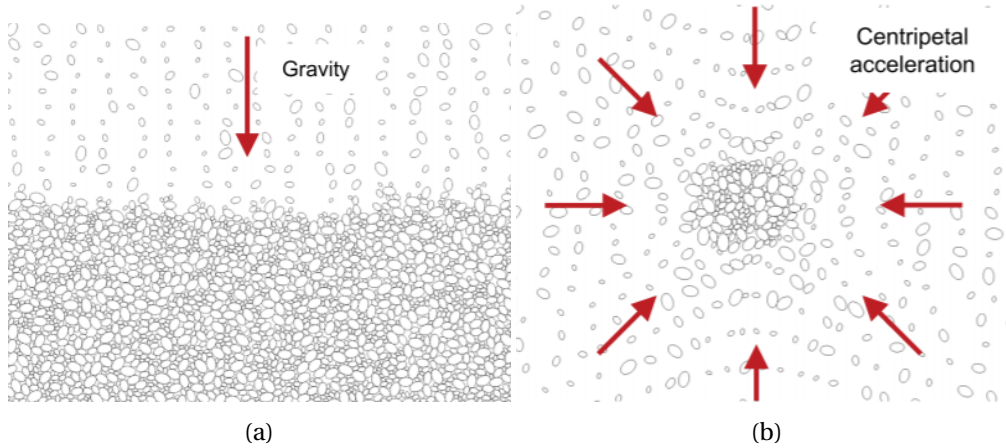
Figure 2.2: Visualization of different fabric due to (a) gravity and (b) centripetal acceleration (Wang et al., 2017).

Specific Gravity

The grain density is defined as the average density of the solid particles in the soil, given by Equation (2.1).

$$\rho_s = \frac{m_s}{V_s} \tag{2.1}$$

Where m_s indicates the mass of solid particles and V_s the volume of solids. The specific gravity of particles is given by Equation (2.2).

$$G_s = \frac{\rho_s}{\rho_w} \tag{2.2}$$

Where ρ_w is the density of distilled water, approximately equal to $1000 \, kg/m^3$

Void Ratio

In between the particles of a granular material there are voids, which are filled with a liquid or a gas. The relationship between pores and solids is described by the term void ratio, e, (2.3). Some literature also uses the term porosity, n (2.4). These variables may be decisive for the deformation behavior of a soil. The ratios e and n are considered simple fabric descriptors, characterizing how densely the particles are packed.

$$e = \frac{V_p}{V_s} = \frac{n}{1 - n} \tag{2.3}$$

$$n = \frac{V_p}{V} \tag{2.4}$$

In Equation (2.3) and (2.4) V_p represents the volume of pores and V the total volume of the soil. From the void ratio, another material parameter can be derived. The relative density of a soil is given as

$$D_r = \frac{e_{max} - e}{e_{max} - e_{min}} \tag{2.5}$$

Where e_{max} gives the void ratio in the soils loosest possible state, and e_{min} the void ratio in its densest state. An additional way to describe the relationship between pores and solids in a soil is by the specific volume, Equation (2.6).

$$v = \frac{V_p + V_s}{V_s} = 1 + e \tag{2.6}$$

Dilatancy

When densely packed grains are subjected to shear stresses, the grains must climb on top of each other in order to move. This leads to a volume expansion, also known as dilation. On the contrary, if loosely packed grains are subjected to the same shear stresses, the grains will fall in between each other. Hence the volume will decrease, which is known as contraction. The materials ability to change in volume when subjected to shear stresses is known as the dilatancy angle, ψ (Figure 2.3).

2.2 Triaxial Testing

The triaxial test has long been the most common laboratory test to determine properties of granular materials (Bishop and Henkel, 1962). It is one of the most widely performed tests to make assessments on shear strength and stiffness properties on soils for geotechnical design. The main test principle is to
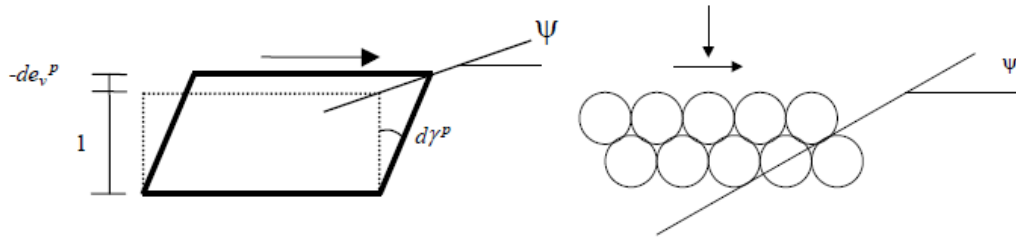
Figure 2.3: Dilatancy occur when densely packed grains climb on top of each other (Nordal, 2020).

approximate a sample's in situ stress condition by applying a three-dimensional stress condition on the sample. The 3-D stress condition is described by the principal stresses σ_1 and $\sigma_2 = \sigma_3$. A triaxial test can be performed passive (extension), but is most commonly conducted active (compression).

2.2.1 The Test Procedure

Consolidation Phase

If the triaxial test is conducted consolidated, a consolidation stage is required. An assembly of a granular material, a specimen, is confined by a rubber membrane. The test is then conducted by placing the specimen into a cell filled with a fluid. When the cell fluid surrounding the specimen is pressurized, confining pressure, $\sigma_1 = \sigma_2 = \sigma_3$, is applied in order to approximate the actual in-situ condition of the soil. If the applied stresses in all directions are equal, the consolidation is called isotropic. The stress state is said to be anisotropic whenever the confining pressure differs from the axial stress.

An unconsolidated triaxial test can be conducted if it is desired to address soil stability of cohesive soil samples in terms of undrained (short term) shear strength. Then the consolidation stage is skipped.

Shear Phase

Following the consolidation stage is the shear stage, where the sample is subjected to deviatoric stresses, i.e. $\sigma_1 \neq \sigma_3$, and shear stresses occur. This loading may be either monotonic or cyclic. Further, the axial load may be applied with closed or open pore water tubes creating undrained and drained conditions respectively.

Stresses and strains in the sample are calculated by monitoring the axial loading, cell pressure and deformations at the physical boundaries. Thereafter, the strength and stiffness parameters can be derived. These results may be presented using different types of stress plots, depending on which features are being investigated. The stresses are usually separated between mean stress, p (2.7), and deviatoric stress, q (2.8) in the triaxial space. That is to keep the volumetric and the deviatoric stress-strain effects apart.
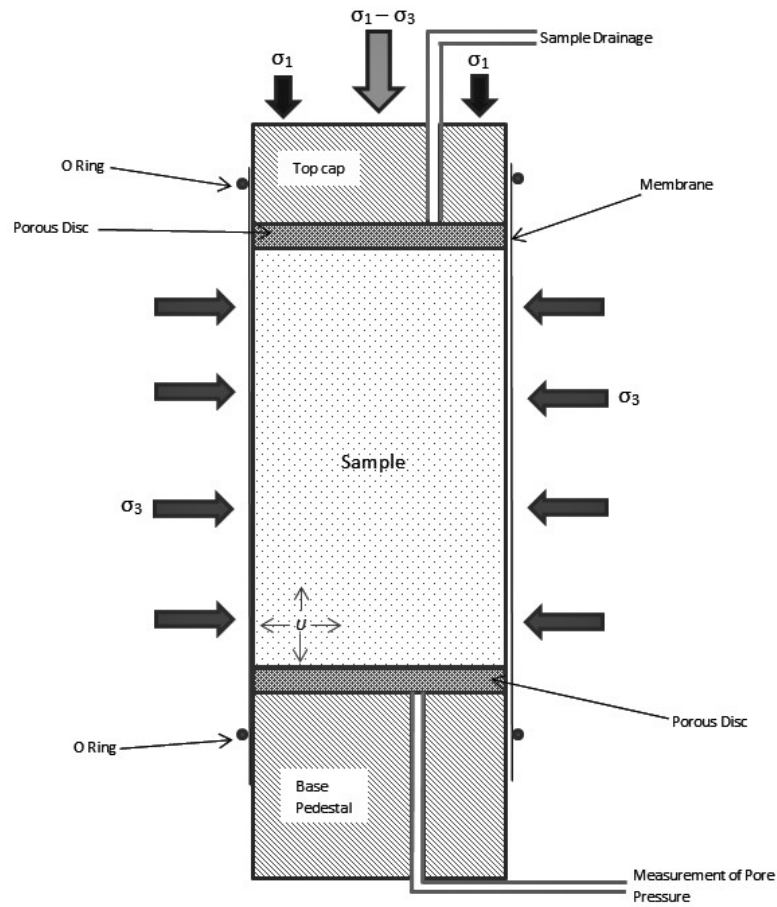
Figure 2.4: Stress conditions in a typical triaxial test ("Triaxial Testing - an Introduction", 2017).

$$p = \frac{1}{3}(\sigma_1 + \sigma_2 + \sigma_3) = \frac{1}{3}(\sigma_1 + 2\sigma_3) \tag{2.7}$$

$$q = \sigma_1 - \sigma_3 \tag{2.8}$$

There are mainly three types of triaxial tests conducted in the laboratory:

- Unconsolidated Undrained test (UU)

- Consolidated Undrained test (CU)

- Consolidated Drained test (CD)

The tests can be conducted either as compression tests ($\sigma_1 > \sigma_2, \sigma_3$) or extension tests ($\sigma_1 < \sigma_2, \sigma_3$) The general set-up for a soil specimen inside a triaxial cell is shown in Figure 2.4.

2.2.2   Sample Preparation

While there exists a number of techniques to obtain high quality cohesive soil samples for laboratory testing, there are still very few ways to obtain undisturbed cohesionless samples. Therefore, most triaxial testing on sand rely on preparing reconstituted sand samples. An important factor influencing the stress-strain behavior of such samples is the structural arrangement of the grains, the fabric, which is strongly affected by the sample preparation method. Since the chosen method greatly impacts the soils response, it should strive to resemble reality. The preparation methods dry and moist tamping as well as dry and moist pluviation are most commonly used. Dry tamping and dry pluviation are described below.

Dry tamped samples are prepared with air dry sand in a mold, using a tamping rod attached to a circular footing. The samples are prepared with a specified amount of layers and amount of blows per layer, as well as a given drop height of tamper. The goal is to obtain a uniform sample, where each layer is tamped to a desired density (Raghunandan et al., 2012).

In dry pluviation, sand samples are prepared to a specified initial state as air dry sand is uniformly rained through a funnel placed above a mold. While the cylinder is filled, a rubber rod taps the cylinder in order to reach higher density. The pluviation is periodically stopped, so that the density reached can be verified. This sample preparation method can be performed by clamping the funnel at a fixed height above the mold, or by fixing the height of the fall of the sand particles (Raghunandan et al., 2012).

2.2.3   Drainage Conditions

An external total stress change is applied on a soil sample during a non-dry triaxial test. Following, the pore water pressure in the specimen changes as well. The drainage condition controls whether this pore water pressure can dissipate or not. Undrained conditions implicate that dissipation of excess pore pressure is prevented, and accordingly the volume change will be zero. As for a fully drained condition, the excess pore water pressure dissipates. No excess pore water pressure develops, and therefore effective stresses will equal the total stresses.

2.2.4   Limitations with Triaxial Testing

None of the available methods for sample preparation have shown to be very consistent. Accordingly will the same specimen preparation method yield varying initial fabric. This will in turn affect the soils mechanical response during testing. Therefore, selecting the most suitable method is challenging. Stress probing is referred to as the cornerstone of experiments on granular materials (Karapiperis et al., 2020). This method aims to achieve several different stress paths from an identical state, which have shown to be extremely difficult to do in the lab, due to the aforementioned limitations with physical sample preparation.

The specimens tested are considered representative elements for describing the soil. Inhomogenities induced by the boundary conditions of the test are neglected, even though several past studies have shown that they may in fact influence the test results (Salvatore et al., 2018; Lam and Tatsuoka, 1988). In addition, conventional triaxial testing measures forces and deformations at the boundaries, assum-
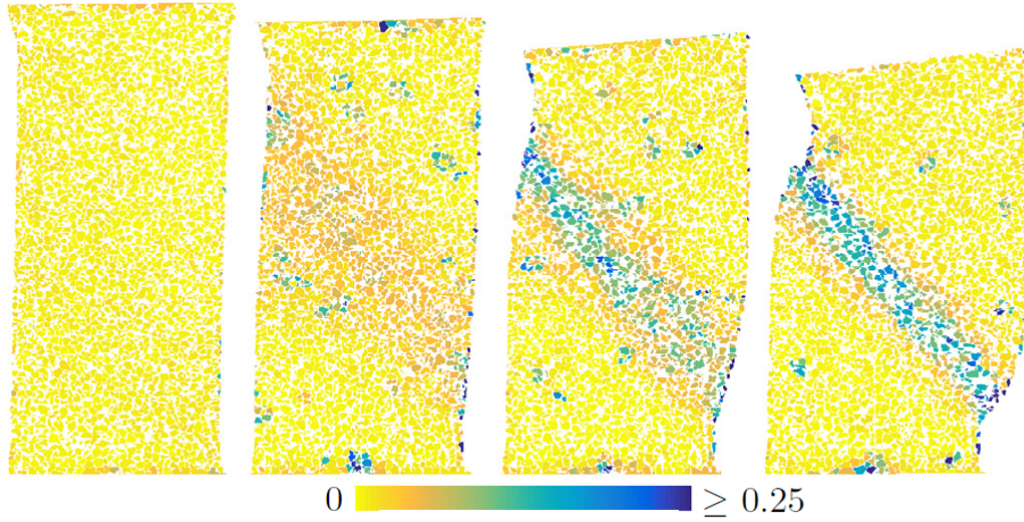
Figure 2.5: The evolution of shear band in a triaxial test. Shades showing incremental local deviatoric strain at different levels of axial strain.

ing that these are uniformly distributed throughout the sample. However, following this assumption, the distinct nature of granular soils is ignored. In practice, the test results only give a macroscopic average of the complex microscopic particle behavior. This is, in some cases, a considerable approximation, especially when going to large strains. The strains will then localize in relatively narrow regions of the sample, leaving the rest more or less undeformed. This phenomena is called strain localization. During triaxial compression, the strains will often localize in an inclined band in the sample (Figure 2.5). This band is referred to as a shear band. The inhomogeneous behavior will affect the macroscopic response measured on the boundaries.

2.3 Continuum Material Models

2.3.1 Elasticity

Hooke's law of elasticity describes a linear relationship between stresses and strains. The elastic strains are, by definition, reversible. Hooke's law is given in Equation (2.9), and yields that the increment in elastic strains is given by the load increment in terms of stress increment, divided by the elastic modulus, E.

$$\Delta \varepsilon^e = \frac{\Delta \sigma}{E} \tag{2.9}$$

Here, the superscript e refers to elastic strains. The isotropic linear elastic stiffness can either be described by the elastic modulus E and the Poissons' ratio v, or the derived parameters K and G (Equation (2.10) and (2.11))

$$K = \frac{E}{3(1-2v)} \tag{2.10}$$

$$G = \frac{E}{2(1+v)} \tag{2.11}$$

K is recognized as the bulk modulus and controls the stiffness related to elastic volume change, while the shear modulus, G, controls the stiffness related to elastic change in shape. Accordingly, elastic volumetric and shear strain increments are proportional to respectively volumetric and shear stress increments, as given in Equation (2.12) and (2.13).

$$\Delta \varepsilon_V^e = \frac{1}{K} \Delta p \tag{2.12}$$

$$\Delta \gamma^e = \frac{1}{G} \Delta \tau = \frac{1}{2G} \Delta q \tag{2.13}$$

2.3.2 Plasticity

For granular materials, plasticity (non-reversible deformation of a material) is partly due to rearrangement of particles. Crushing of grains will also lead to plastic deformation, but this is not considered in this thesis.

When applying stress higher than the yield limit, plastic strains will develop. Following this, the yield criterion is often recognized as a limiting surface, F, in the stress-space. Stress increments inside the limiting surface, $F < 0$, give elastic strains ε^e, while stress increments on the yield surface, $F = 0$, make the material yield and give permanent strains ε^p.

How the plastic strains develop when the stress level is increased beyond a yield limit is described by a plastic flow rule. A plastic strain increment proportional to the plastifying stress increment gives associated flow. Hence, in cases of associated flow, the plastic strain have the same direction as $d\sigma^p$ in the stress-space. Accordingly, the direction of the plastic strain increment is defined by normality to the yield surface (2.14).

$$d\varepsilon^p = \begin{bmatrix} d\varepsilon_1^p \\ d\varepsilon_3^p \end{bmatrix} = d\lambda \begin{bmatrix} \frac{\partial F}{\partial \sigma_1} \\ \frac{\partial F}{\partial \sigma_3} \end{bmatrix} \tag{2.14}$$

Here, λ is the plastic multiplier scalar. It is determined by ensuring that the stress state satisfies $F = 0$ during plastic flow.

Associated flow is usually a correct assumption when considering metals, but has shown to be inaccurate in the consideration of soils. In particular, it has a tendency to overestimate the plastic volume expansion. Accordingly, when considering soils, non-associated plastic flow often yields a better prediction. In cases of non-associated flow, the plastic flow is not perpendicular to the yield surface, and a plastic potential surface, Q, is introduced. Accordingly, the flow rule is given as in Equation (2.15) (Salecon, 1974).

$$d\varepsilon^p = \begin{bmatrix} d\varepsilon_1^p \\ d\varepsilon_3^p \end{bmatrix} = d\lambda \begin{bmatrix} \frac{\partial Q}{\partial \sigma_1} \\ \frac{\partial Q}{\partial \sigma_3} \end{bmatrix} \tag{2.15}$$

2.3.3 Elasto-Plasticity

Elastic-plastic material models are based on the assumption that total strains can be separated into elastic strains, ε^e, and plastic strains, ε^p (Irgens, 2008). There are multiple ways to idealize an elasto-plastic material. Four different models are visualized in Figure 2.6.

(a) Rigid perfectly plastic.

(b) Elastic perfectly plastic.

(c) Elastic-plastic hardening.

(d) Elastic-plastic softening.
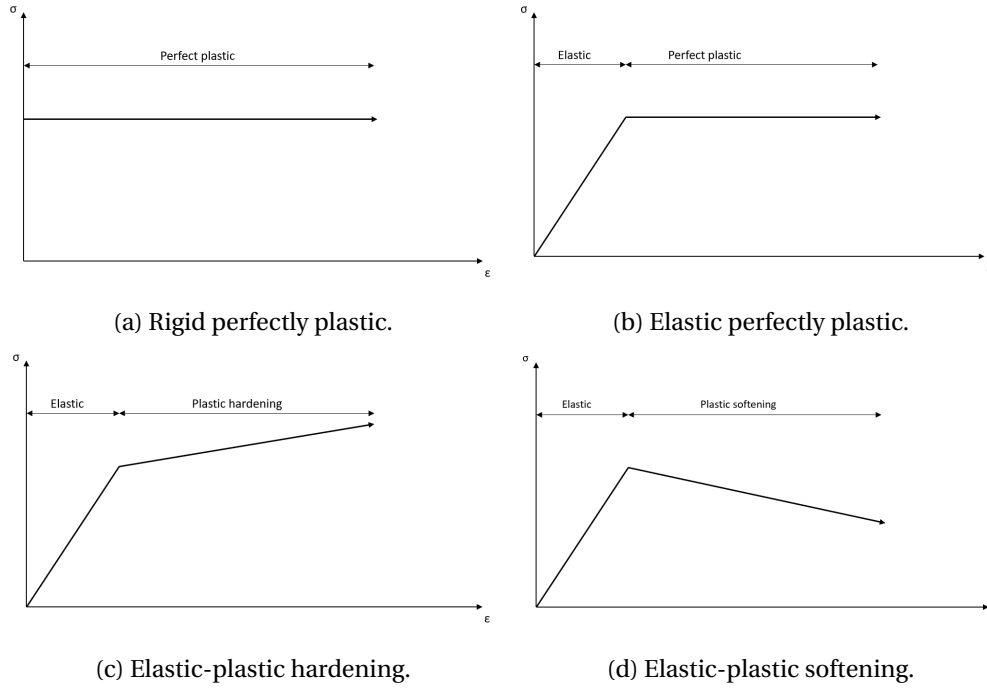
Figure 2.6: Idealization of elasto-plastic behavior.

Figure 2.6b shows linear elastic perfectly plastic behavior, which is the simplest elasto-plastic model. This behavior involves no hardening nor softening in the material. These phenomena are however illustrated in Figure 2.6c and 2.6d respectively. When the stress level is below the failure line, F, elastic strains will develop. Loading on the failure line yields plastic strains, while loading over the failure line is not possible. Unloading gives elastic response. The elastic response, as well as the plastic hardening and softening, are visualized as linear in Figure 2.6 for simplicity, but this does not have to be the case.

2.3.4 Critical State Soil Mechanics (CSSM)

As described in Section 2.1, a soil will, depending on how densely it is packed, either expand (dilate) or contract when subjected to shear stresses. Experiments have shown that grains in both loosely and densely packed samples will rearrange until reaching the same critical void ratio (Schofield and Wroth, 1968). For large strains, this void ratio is considered unique for the selected average pressure, p. No volumetric strain will occur after reaching this state. Following this, a critical state (CS) is defined as a

state where large strains may be applied without any change in effective stresses or in volume (Wood, 1991). The concept is illustrated in Figure 2.7. Recent research shows that not only stress and void ratio, but also fabric, is unique at critical state (X. S. Li and Dafalias, 2012), independent of initial fabric. This extension to the critical state theory is called Anisotropic Critical State Theory (ACST). Wang et al. (2017) shows that all three aforementioned fabric tensor categories reaches a unique critical state fabric tensor.
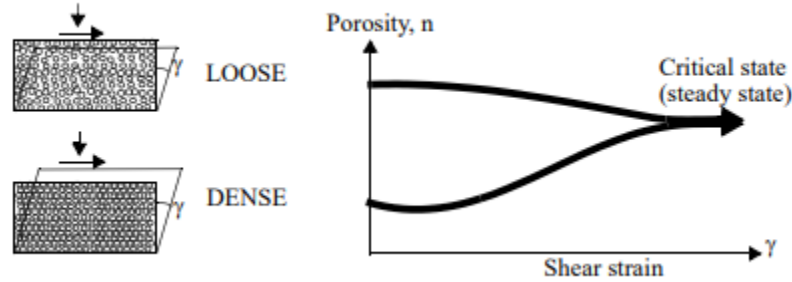
Figure 2.7: A loose and a dense soil sheared until critical state is reached (Schofield and Wroth, 1968).

The classical critical state may be defined by a set of two equations. Equation (2.16) and (2.17) are illustrated in Figure 2.8a and 2.8b respectively.

$$q_c = Mp \tag{2.16}$$

$$\Gamma = v_c + \lambda \ln(p) \tag{2.17}$$

$$v_c = 1 + e_c \tag{2.18}$$
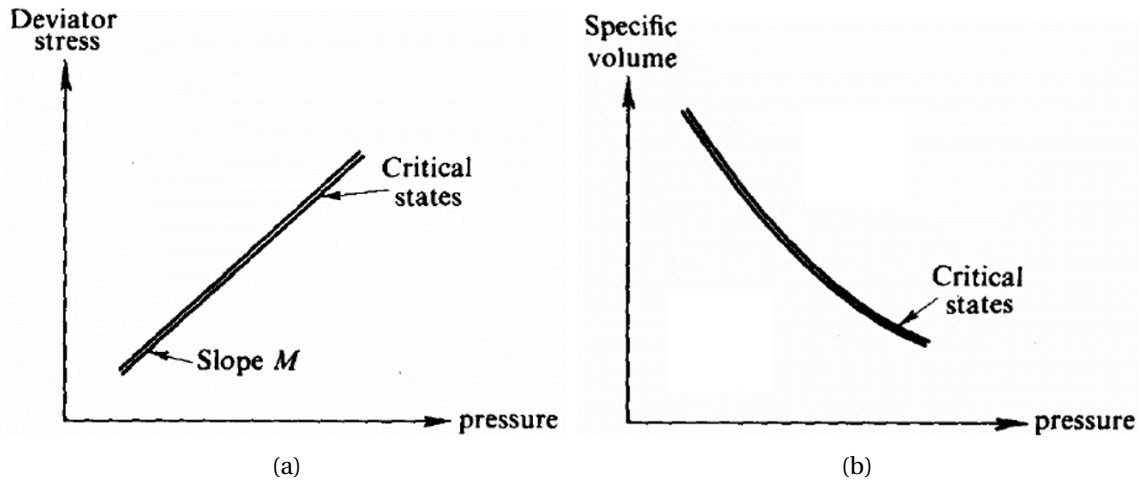
Figure 2.8: Critical states adapted from (Schofield and Wroth, 1968).

Here, q_c is the critical deviatoric stress and p the mean stress. M is the critical stress ratio, given as a material parameter. Γ and λ are soil constants, and v_c the critical specific volume, given by Equation

2.18.

The critical void ratio will decrease with an increase in average pressure (Casagrande, 1979). A critical state line (CSL) describes the combination of average pressure and critical void ratio at which shearing of a soil may continue infinitely. For an initial void ratio lower than the CSL, the void ratio will increase during shearing (dilation), and for an initial void ratio higher than CSL, the void ratio will decrease (contraction). Note that Equation (2.17) is just a mathematical representation of the critical state line, and other equations may be used. SANISAND introduce an exponent, and uses Equation (2.23) for the location of the critical state line.

Limitations with CSSM

The critical state is assumed independent of the loading path. Accordingly, specimens should reach the same critical void ratio under both triaxial compression and triaxial extension. However, this does not coincide well with experimental data, where extension tests tend to reach a lower critical void ratio than compression tests (Salvatore et al., 2017). This discrepancy is eliminated when the void ratios are computed only within the limited area of large deformations. As commented in Section 2.2, large deformations often appear in narrow regions of the sample, as so-called strain localization. When the critical void ratios are measured only within these regions, the critical state is independent of the stress path (Figure 2.9). This may indicate that the strain localization develops differently for triaxial extension and compression. Further, it implies that conventional laboratory testing is insufficient in measuring the critical state parameters because of their inability to capture the inhomogeneous deformation within a specimen. As a consequence, it is difficult to calibrate a unique set of input-parameters for a critical state based constitutive material model only by using conventional laboratory test results.
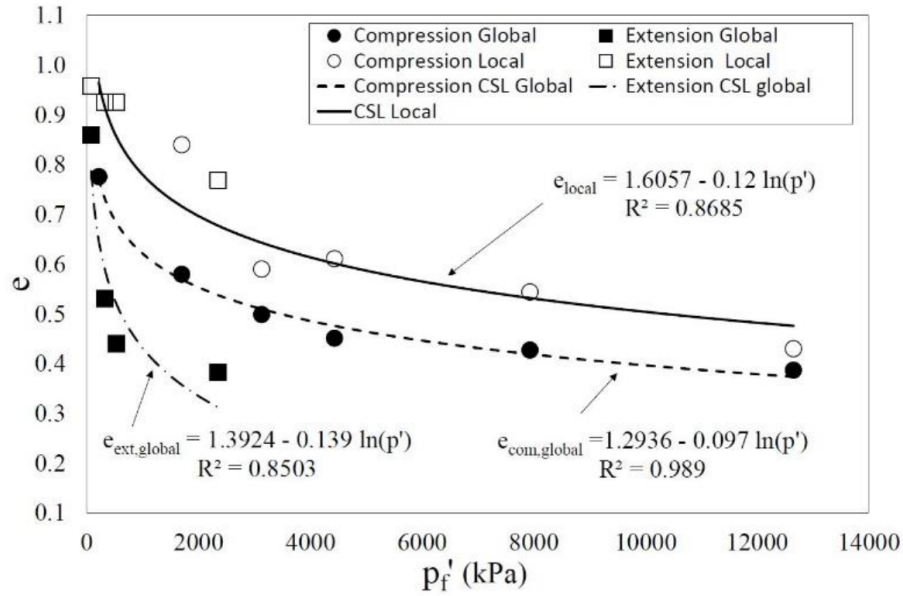
Figure 2.9: Representation of the volumetric state at the end of compression and extension tests (Salvatore et al., 2017).

2.3.5 Bounding Surface Plasticity

The classical yield surface plasticity formulation often assumes an elastic range too big compared to experimental data (Yu, 2006). In addition, the sudden change from elastic to plastic strains described by the classical formulation deviates from the gradual change in stiffness observed in experimental results. This especially limits the classical formulations ability to capture the material response when subjected to cyclic loading.

The concept of a bounding surface in the stress space was first introduced for metals, and later extended to yield for different materials as well, such as soils (Dafalias, 1986). The framework proposes a smooth transition from elastic to plastic strains, by the use of a mapping rule for any stress state below or on the bounding surface. The mapping rule associates the actual stress state with a corresponding "image" stress point on the bounding surface, and measures the distance between the actual and image stress to specify the plastic modulus (Dafalias, 1986). The bounding surface evolves as the soil is deformed, and is therefore not considered a critical state.

Different shapes of the bounding surface are proposed in different literature. In the SANISAND model (Taiebat and Dafalias, 2008), a straight line is used.

2.4 SANISAND

SANISAND is the name used for a family of Simple ANIsotropic SAND constitutive models within the framework of critical state soil mechanics and bounding surface plasticity. The following section gives

a summary of the main features of the model, which is based on the model presented in (Taiebat and Dafalias, 2008) where not explicitly stated otherwise. All stresses are considered effective. For a more thorough understanding of the model, readers are referred to (Taiebat and Dafalias, 2008).

SANISAND was developed to simulate the complex stress-strain behavior of sand in both monotonic and cyclic, drained and undrained loading. It incorporates a unique set of input parameters for a given sand, independent of relative density. This is considered an important advantage compared to simpler models, which often treats the same sand at different states as different materials. The input parameters are normally calibrated from conventional laboratory testing. Hence, microscopic parameters such as grain size distribution and grain shape are not explicitly incorporated in the model but is implicitly captured by the macroscopic response of the material.

The model describes a mean stress-dependent critical state formulation. Further, the elastic shear modulus, G (2.21), is given by an equation dependent on p and e, together with a dimensionless input parameter G_0. The elastic bulk modulus, K (2.22), is dependent on the elastic shear stiffness together with Poisson's ratio, v, and the model parameter K_0.

Earlier versions of the model, such as (Dafalias and Manzari, 2004), claims that only change in the stress ratio $\eta = q/p$ can cause relative shearing and rolling of grains, which macroscopically is modeled as plastic shear- and volume deformation. Hence, loading with a constant stress ratio will only cause elastic deformation. Taiebat and Dafalias (2008) extended the model to include an additional yield surface allowing for plastic volumetric deformation also for loading at a constant stress ratio. This allows for capturing plastic contraction caused by rearrangement of grains for a loosely packed sample under isotropic compression, as well as crushing of grains for a densely packed sample. The latter is not considered in this thesis.

In the latest version, the yield surface is recognized as a narrow wedge with a cap-like tip in the $p - q$ space (Figure 2.10). The narrowness of the elastic regime is necessary to capture the effect of loading reversals, including cyclic loading. Half the opening of the wedge is given by the input parameter m. The cap of the surface is found at $p = p_0$. With the new implementation, a new stress quantity was introduced: the back stress ratio, α. It can be shown that as p varies from zero to p_0, α^c varies from $\alpha^c = M - m$ to $\alpha^c = M$. Here, α^c indicates the back-stress ratio at critical state, and M a material parameter giving the slope of the critical state surface in the $p - q$ space. Due to the narrowness of the wedge, m is considerably smaller than M; typically set to $m = 0.05\alpha^c$ (Papadimitriou et al., 2001). Hence, the substitution of α for η in critical state creates no significant error.

The ratio between plastic volumetric and deviatoric strain, the dilatancy, depends on the distance from the current stress-state to the dilatancy surface. It also depends on an input parameter, A_d. The material contracts inside the surface and dilates outside. In (Dafalias and Manzari, 2004), a fabric-dilatancy related quantity is introduced to account for the macroscopic effect related to fabric changes. During the dilatant phase of plastic deformation, the grains rearrange resulting in a drastic change in fabric. This change has an impact on the contractant response during unloading. It is important to capture in order to accurately model the soils response, especially during undrained cyclic loading. Therefore, the dilatancy expression is made to depend on a fabric-dilatancy scalar whose evolution models macroscopically

the effect of fabric changes.

2.4.1   Formulation in Triaxial Space

The SANISAND equations in this section are formulated in the triaxial stress space, with all components considered as effective stresses. Deviatoric and volumetric stresses are as given in Section 2.2. Devatoric strain, ε_q, and volumetric strain, ε_v are as given in Equation (2.19).

$$\varepsilon_q = \frac{2}{3}(\varepsilon_1 - \varepsilon_3); \qquad \varepsilon_v = \varepsilon_1 + 2\varepsilon_3 \tag{2.19}$$

Elastic relations

The incremental stress-strain relation for elastic deformations are given in Equation (2.20). G and K are as given in Equation (2.21) and (2.22).

$$d\varepsilon_q^e = \frac{dq}{3G}; \qquad d\varepsilon_v^e = \frac{dp}{K} \tag{2.20}$$

$$G = G_0 p_{atm} \frac{(2.97 - e)^2}{1 + e} \left(\frac{p}{p_{atm}}\right)^{1/2} \tag{2.21}$$

$$K = K_0 p_{atm} \frac{1 + e}{e} \left(\frac{p}{p_{atm}}\right)^{2/3} = \frac{2(1 + v)}{3(1 - 2v)} G \tag{2.22}$$

Yield, critical, bounding and dilatancy surfaces

The location of the critical state line, e_c, in the $p - e$ space is given by Equation (2.23) (X. S. Li and Wang, 1998).

$$e_c = e_0 - \lambda \left(\frac{p_c}{p_{atm}}\right)^{\xi} \tag{2.23}$$

Where e_0, λ and ξ are constants. e_c and p_c indicates the critical void ratio and confining pressure respectively.
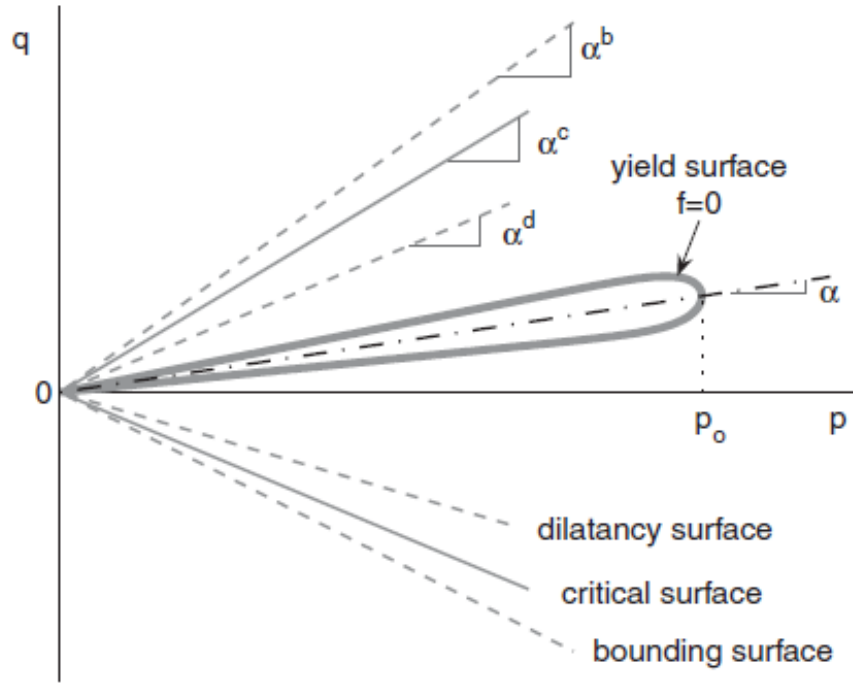
Figure 2.10: Schematic illustration of model surfaces in triaxial space (Taiebat and Dafalias, 2008).

The yield surface is visualized in Figure 2.10 and given by Equation (2.24).

$$f = (q - p\alpha)^2 - m^2 p^2 \left[1 - \left(\frac{p}{p_0} \right)^n \right] = 0 \tag{2.24}$$

In addition to the yield and critical surfaces, two other surfaces are incorporated in the model; the bounding and the dilatancy surface. The inclination of the critical state surface, α^c, in the $p - q$ space is taken as an input parameter. The bounding and dilatancy surfaces, α^b and α^d, are given as functions of respectively a bounding and dilatancy constant. They are related to the CSL through the state parameter, ψ, where ψ is the distance between the current void ratio and the critical void ratio, $\psi = e - e_c$ (Figure 2.11). Equations (2.25) and (2.26) give respectively the bounding and the dilatancy surface (X. S. Li and Dafalias, 2000).

$$\alpha_c^b = \alpha_c^c exp(-n^b \psi) \tag{2.25}$$

$$\alpha_c^d = \alpha_c^c exp(n^d \psi) \tag{2.26}$$

Here, the superscripts c, b and d refers to respectively critical, bounding and dilatancy surface. Further, the subscript c refers to triaxial compression. For extension, the input scalar $c = \alpha_e^c / \alpha_c^c$ is used.

For the bounding surface formulation, it is necessary to define an "image" of a stress quantity onto a bounding or a similar surface. For the critical surface in triaxial space, the image of the current back-
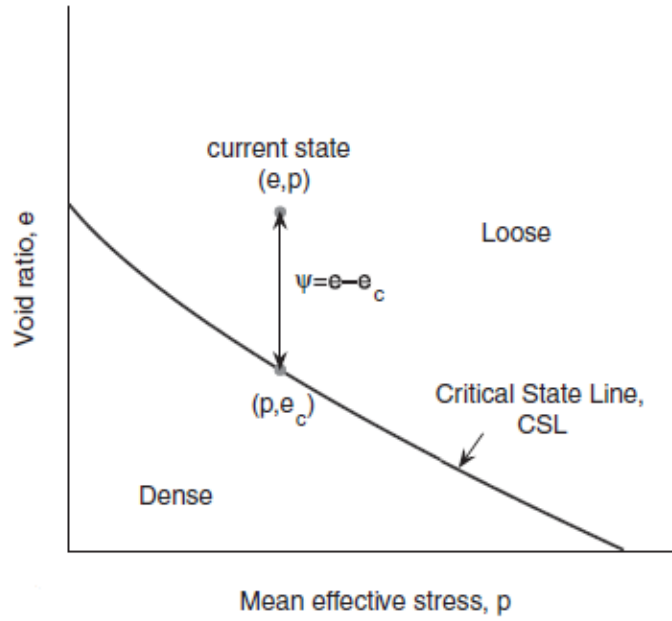
Figure 2.11: Schematic illustration of CSL and ψ (Taiebat and Dafalias, 2008).

stress ratio, α, on the critical surface is $\alpha^c = \alpha_c^c$ when $\eta - \alpha > 0$ and $\alpha^c = -\alpha_e^c$ when $\eta - \alpha < 0$. Similar rules yields for the bounding and dilatancy surfaces.

Flow Rule

The evolution of plastic deviatoric and volumetric strains are given as in Equation (2.27 - 2.29). The expressions are decomposed into two contributions, indicated by subscripts 1 and 2. In the following, it is assumed that p is far away from the tip, hence only the first contribution is practically active and $r_{ef} \simeq m$. $s = 1$ for triaxial compression.

$$\dot{\varepsilon}_q^p = (\dot{\varepsilon}_q^p)_1 + (\dot{\varepsilon}_q^p)_2 = \langle L \rangle [s r_{ef} + X \eta e^{-V r_{ef}}] \simeq \langle L \rangle m \tag{2.27}$$

$$\dot{\varepsilon}_v^p = (\dot{\varepsilon}_v^p)_1 + (\dot{\varepsilon}_v^p)_2 = \langle L \rangle [D r_{ef} + e^{-V r_{ef}}] \simeq D \dot{\varepsilon}_q^p \tag{2.28}$$

$$r_{ef} = |\eta - \alpha| = \left[1 - \left(\frac{p}{p_0} \right)^n \right]^{1/2} \simeq m \tag{2.29}$$

Where L is the positive plastic loading index, or the plastic multiplier, and V is considered high, default $V = 1000$. D refers to the dilatancy, given as a function of the distance $\alpha^d - \alpha$ and the dilatancy parameter, A_d (2.30).

$$D = s A_d (\alpha^d - \alpha) \tag{2.30}$$

The evolution of α can be written as a function of h which is a function of b_0, as given in the following:

$$\dot{\alpha} = \langle L \rangle h |\eta - \alpha| (\alpha^b - \alpha) = \langle L \rangle h r_{ef} (\alpha^b - \alpha) \tag{2.31}$$

$$h = \frac{b_0}{(b_{ref} - s(\alpha^b - \alpha))^2} \tag{2.32}$$

$$b_0 = G_0 h_0 (1 - c_h e) \left(\frac{p_{atm}}{p} \right)^{1/2} \tag{2.33}$$

Here, $b_{ref} = \alpha_c^b + \alpha_e^b$, such that for $s = 1$ and $\alpha^b = \alpha_c^b$, $b_{ref} - s(\alpha^b - \alpha) = \alpha_e^b + \alpha$. c_h and h_0 are positive input parameters for the SANISAND model.

A summary of the formulation in triaxial space is given in Table 2.1.

Table 2.1: Triaxial formulation of the SANISAND model (Taiebat and Dafalias, 2008).

	Triaxial formulation
Elasticity	$\dot{\varepsilon}_q^e = \dot{q}/(3G)$ $\dot{\varepsilon}_V^e = \dot{p}/K$
Yield surface	$f = (q - p\alpha)^2 - m^2 p^2 [1 - (p/p_0)^n] = 0$
Flow rule	$\dot{\varepsilon}_q^p = \langle L \rangle [s r_{ef} + X\eta e^{-V r_{ef}}]$ $\dot{\varepsilon}_V^p = \langle L \rangle [D r_{ef} + e^{-V r_{ef}}]$ $r_{ef} = |\eta - \alpha|$
Evolution laws	$\dot{\alpha} = \langle L \rangle h (\alpha^b - \alpha) r_{ef}$ $\dot{p}_0 = \langle L \rangle p_0 (1 + e) e^{-V r_{ef}} / [e(\rho_c - (p_0/p_{atm})^{1/3}/K_0)(1 - sgn\delta |\delta^\theta|)]$ $h = b_0 / [b_{ref} - s(\alpha^b - \alpha)]^2$ $D = s A_d (\alpha^d - \alpha)$ $s = (q - p\alpha)/|q - p\alpha|$ $\alpha^{c,b,d} = s g \alpha_c^{c,b,d}$ $\alpha_c^b = \alpha_c^c \exp(-n^b \psi)$ $\alpha_c^d = \alpha_c^c \exp(n^d \psi)$
Yield surface derivatives	$\delta f / \delta p = -2\alpha(q - p\alpha) - 2m^2 p + (2 + n) m^2 p (p/p_0)^n$ $\delta f / \delta q = 2(q - \alpha p)$ $\delta f / \delta \alpha = -2p(q - \alpha p)$ $\delta f / \delta p_0 = -(n/p_0) m^2 p^2 (p/p_0)^n$

2.4.2 Calibration of SANISAND Input Parameters

In the SANISAND model, the material is defined by the 16 input parameters stated in Table 2.2. Many of the parameters can be determined from standard laboratory testing, such as drained and undrained

triaxial compression and extension tests (Taiebat and Dafalias, 2008). The calibration is mostly done by curve-fitting.

Due to the large number of input parameters, results from several tests are necessary to obtain a complete set of parameters. This includes triaxial tests of samples from different pressure levels and from different initial void ratios. It is also recommended to include both drained and undrained analyses in the calibration process.

Table 2.2: Input parameters for the SANISAND model

	Parameter
Elasticity	G_0
	K_0
CSL	α_c^c
	c
	e_0
	λ
	ξ
Yield Surface	m
Dilatancy	n^d
	A_d
Kinematic hardening	n^b
	h_0
	c_h
Fabric-dilatancy tensor	z_{max}
	c_z
Limiting compression curve (LCC)	p_r
	ρ_c
	θ
	X

2.4.3   Limitations with SANISAND

One of the most important drawbacks of advanced soil models like SANISAND, is the excessive lab work necessary to calibrate the input parameters. In addition, it is difficult to get a unique set of parameters for one given type of sand. Some parameters are calibrated using a trial-and-error approach. These are particularly challenging to uniquely define, as several combinations may yield good fits with the experimental data. In addition, the best fit for one type of stress path may not be the best fit for another path.

Even though SANISAND is able to replicate soil behavior with a high order of accuracy in most load cases, the model have shown to have some shortcomings, especially when it comes to cyclic loading. Jostad et al. (2020) advises against using the current version SANISAND to predict the effect of cyclic loading of an OWT foundation in dense sand. That is due to its shortcomings when it comes to modeling a soils response to cyclic loading.

Chapter 3

Discrete Element Method

3.1 Traditional DEM

An alternative to the continuum approach is to numerically model the sand as an assembly of distinct particles interacting with each other. In this way, the model can explicitly reproduce the nature of discontinuity that is characteristic for a granular material. Such an approach is known as the discrete element method (DEM). The numerical approach allows for calculating quantities not possible to measure in experimental results, such as the interparticle forces between the grains. It is also able to capture the behavior within shear bands as well as individual particle orientation. These quantities are essential when investigating the relationship between sand fabric (micro) and accumulated deformations (macro). This relationship is important to understand to succeed in building a reliable constitutive material model. In addition, several limitations associated with physical testing are eliminated by replacing traditional laboratory testing with DEM simulations. This including the physical boundary conditions as well as the influence of specimen variation (Fu and Dafalias, 2011). It is also easier to apply large displacements to a numerical model, which makes it easier to identify a well defined critical state line.

The discrete element model was developed in 1979 (Cundall and Strack, 1979). The forces acting on the virtual boundaries of a sample and the displacement of these are calculated by tracking the movements of particles and the forces between them. Contact forces are calculated by allowing the particles to overlap, where forces are quantified by the overlap, using the constitutive model, or the stiffness, of the material. After the forces are calculated for each contact point of each particle, an explicit time integration scheme is used with Newtons laws of motion to update kinematic quantities like velocity, position, and particle orientation for each particle. The process is repeated for a given number of time steps. The size of the time step must be chosen carefully to obtain a proper calculation of the particle movement. Constant accelerations and velocities are assumed at each step, and hence must the time step be small enough to warrant these assumptions.

Usually, such models require a small number of relatively simple input parameters (Fu and Dafalias, 2011). This include material parameters such as normal- and shear stiffness in grain to grain contact, a contact friction coefficient and grain density, together with geometrical parameters describing the shape and size of the grains as well as the fabric. In addition, a model for grain interaction is needed. The

physical material parameters are found with physical testing, as described in Section 3.3. Most DEM codes uses an approximated geometry, often by modeling the grains with simple geometrical shapes.

3.1.1 Contact Formulation

To compute the forces from particle overlap, a constitutive model for grain interaction is necessary. This could be any contact model. For the code run in this thesis, a linear elastic contact model, or a linear spring, is used to model contact normal forces (Kawamoto et al., 2016). Further, a Coulomb friction model is used to model frictional forces. More advanced models for grain interaction may also be implemented, but this would normally require additional material input parameters. However, it is important to remark that DEM is still only a mathematical model aiming at replicating soil behavior, and does not yield a true representation of the nature of granular soils. This is underlined by the necessity of realistic contact models.

3.1.2 Grain Shape

Considerable approximations must be done to describe the complex shape of a grain with simple geometrical shapes. Several variants of DEM have been developed in order to realistically describe grain shape. For instance, the modelling has been done by sphere clumping (Garcia et al., 2009), (Figure 3.1), ellipsoids (Rothenburg and Bathurst, 1991; Yan et al., 2010), (Figure 3.2) and NURBS (Lim and Andrade, 2014), (Figure 3.3). Even though some of these models work acceptably under some conditions, a high order of accuracy comes with a great computational cost. More promising results have been obtained with the Level Set Discrete Element Method (LS-DEM). This variant models the true shape of the grains with high orders of accuracy, and yet keeps the computational costs at acceptable levels.
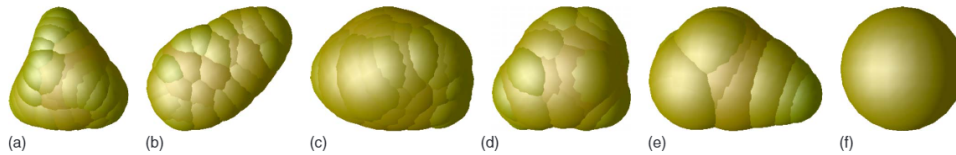
Figure 3.1: Using sphere clumping to represent grain morphology (Garcia et al., 2009).

3.1.3 Critical Time Step

The time step used in the explicit time integration scheme must be small enough to warrant the assumption of constant velocities and accelerations between each calculation. The critical time step is chosen on the basis that during one time step, disturbance cannot propagate from any particles other than its immediate neighbors (Cundall and Strack, 1979). By approximating the interparticle contact as a simple elastic spring, the ordinary differential equation (ODE) can be used as a contact model (3.1).

$$m\frac{\delta^2 d_n}{\delta t^2} + k_n d_n = 0 \qquad (3.1)$$
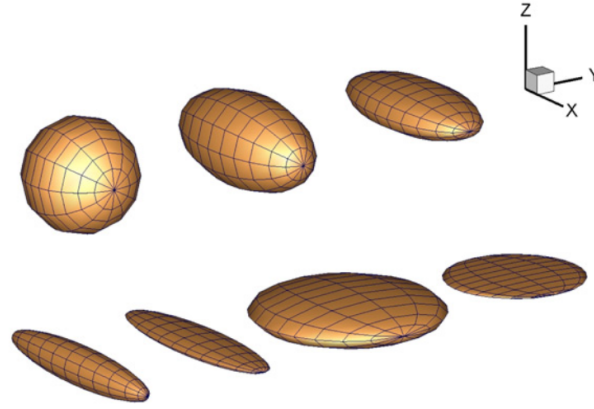
Figure 3.2: Using ellipsoids to represent grain morphology (Yan et al., 2010).
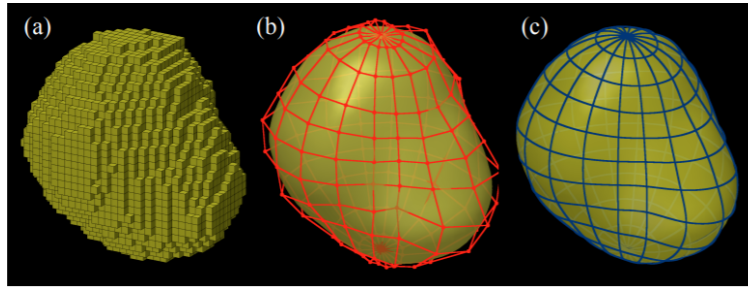
Figure 3.3: Using NURBS to represent grain morphology (Lim and Andrade, 2014).

Where d_n refers to the normal deflection and k_n the normal stiffness in grain-to-grain contact. This equation gives a periodic solution, with a natural period of vibration as given in Equation (3.2)

$$T = 2\pi \sqrt{\frac{m}{k_n}} \qquad (3.2)$$

Where m refers to the mass of the grain. The critical time increment can be defined as half the natural period, $\Delta t_{critical} = T/2$. However, to correctly perform the explicit time integration scheme, it is empirically recommended to use a time step equal to a fraction of this value (3.3).

$$\Delta t = \frac{\Delta t_{critical}}{X} \qquad (3.3)$$

Donze et al. (2009) suggest X equal to $10-20$. However, higher values like $X = 50$ to $X = 100$ are also found in literature. Since no well defined rule on the size of this fraction exists, the time step must be chosen with care.

3.2 LS-DEM

This section is based on (Kawamoto et al., 2018) where not explicitly stated otherwise.

Level Set Discrete Element Method (LS-DEM) uses level set functions to represent the true shape of

the grains. XRCT images of the sample is used with level set imaging (LS-imaging) (Vlahinić et al., 2014) to create mathematical representations of the individual particles. The particles are used in a computational model based on a discrete element framework to simulate sand behavior. The dynamic framework allows the particles to move and interact with each other, and hence the response to external forces can be predicted. To create the numerical particles, an XRCT image of the sand is processed to determine which pixels represent solids and which represent voids. These representations are used together with level-set algorithms (Gao and Chae, 2008; C. Li et al., 2010; Vlahinić et al., 2014) to create "avatars" representing the grains with their specific shape. The level-set functions are implicit functions whose value at a given point is the distance from the point to the surface of the grain. It is positive whenever the point is outside the particle, and negative if the point is inside the particle. Following this, the surface of the grain is described by the points where the level set function is zero. Figure 3.4 illustrates the avatar conversion process for one single avatar in 2D.

In LS-DEM, it is common to separate between two types of analyses: validation and simulation. Here, validation means that an entire sample is scanned after consolidation to create a digital twin. With this method, both grain shape and the initial fabric of the sample is incorporated. To correctly replicate a physical experiment, it is necessary to model the flexible membrane used in conventional triaxial testing, as well as other physical boundary conditions like tilting of the loading platen. For the simulation analyses, already calibrated grains are packed and compressed to reach a specified void ratio and pressure level. With this method, the fabric is randomly generated.
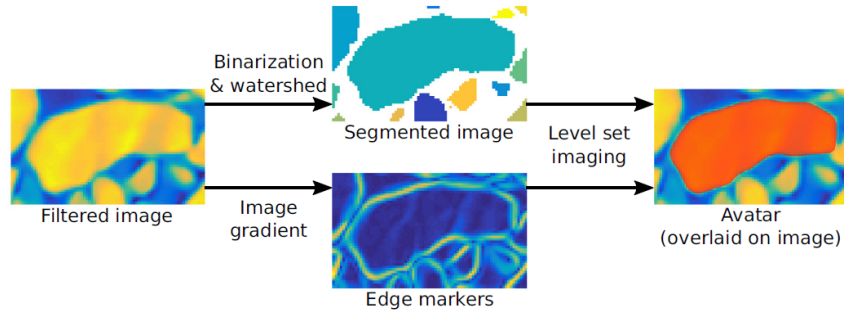
Figure 3.4: Avatar conversion process. The filtered image is both segmented and used to find particle edges. It is then fed into the level set imaging algorithm, which outputs an avatar (from Kawamoto et al., 2018).

A master-slave approach is used to calculate the contact forces in LS-DEM. The master element is discretized into nodes, as visualized in Figure 3.5. Each node of the master element is compared with the level set functions. Whenever the value is negative, contact forces exist. Then the contact forces, as well as updated particle kinematics, are calculated. The number of nodes on the master element is a matter of choice. Since contact is checked for each node, the computational cost will increase with an increasing amount of nodes. According to Kawamoto et al. (2016), a maximum node-to-node spacing of $d/10$, where d is the particle diameter, is adequate to capture the particle morphology.

Figure 3.5: Contact between two particles in LS-DEM. The master element is discretized into nodes. 2D visualization is used for simplicity (Kawamoto et al., 2018).

3.3 Calibration of Input Parameters for DEM

DEM models take physical input parameters such as normal- and shear stiffness in grain-to-grain contact, grain density and a contact friction coefficient as input parameters. In addition, geometrical parameters are needed. T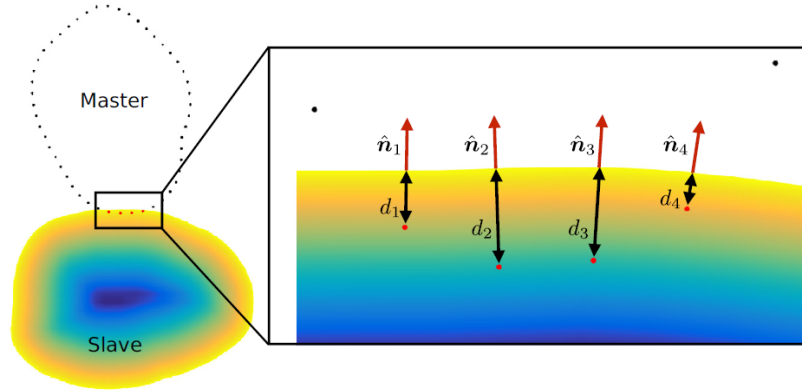his is done by level set functions in LS-DEM or simple geometrical shapes in DEM. The physical parameters are calibrated either by physical testing or by using a digital twin. When using a digital twin, the roughness and contact stiffness is calibrated by running LS-DEM simulations and comparing the results with the experiment.

Some of the physical tests that can be used to calibrate the parameters are proposed in (Nardelli and Coop, 2018). Using an innovative three-axis inter-particle loading apparatus, it is possible to investigate the normal- and shear contact behavior between sand particles. Normal grain stiffness can be obtained by applying vertical loading, usually at a constant displacement rate. The normal load – normal displacement output can be used to determine the normal stiffness, k_n.

The simplest shear test mode is a tangential loading test, where one particle is sheared linearly over the other at a constant displacement rate. From this test, two different types of output are analyzed. The first is the tangential load – tangential displacement output. From which the shear stiffness, k_s, is found, in addition to degradation curve of tangential stiffness with tangential displacement. Second, the coefficient of inter-particle friction, μ, which is defined as the ratio between the tangential force and the normal force applied at the contact once the particles are sliding one over the other.

3.4 Limitations with DEM

One of the most significant drawbacks of the discrete element method is the computational power required to run simulations of relatively small specimens.

Even though the model by nature captures typical behavior of granular soils such as non-associative plasticity and fabric dependency, an appropriate contact model is still necessary to simulate the true

behavior. This is especially important when considering small deformations.

In DEM, it is assumed that the deformation due to the overlap of grains is insignificant compared to deformation due to rearrangement of grains. This assumption yields for most situations. However, when subjected to sufficiently large pressures, such volumetric deformations may become significant.

When using realistic representations of grain shape, such as in LS-DEM, the preparation method of the sample is very important. The preparation is decisive for the initial fabric, which also is especially important when considering small deformations. Initial particle orientation and hence the sample anisotropy is also decided by the packing method.

If a sufficiently small sample is analyzed and rigid boundaries are used, it is possible that the contact forces between grains and the boundaries influence and possibly disturb the geometrical stiffness of the sample. This issue can be avoided by simulating a larger sample, but it may lead to other problems like strain localization, in addition to higher computational costs.

Chapter 4

LS-DEM Simulations

4.1 Implementation

The LS-DEM code has been developed at the California Institute of Technology (Caltech) and is written in C++ programming language. The simulations have been done on Hostun sand, which is a sand characterized by angular and non-spherical grains (Kawamoto et al., 2018). It is therefore prone to showcase the effect of shape on the soil behavior. Further, the simulations are separated into three different stages. The first being a packing stage that builds the specimen, then an isotropic compression stage is run, before the sample is sheared in the final phase.

Three $3x3$ matrices; active strain control, applied strain rate and applied stress are used as input files for each stage in order to control the boundary conditions. The loading can be performed either stress or strain controlled, or a combination of the two. Negative entries in the stress matrix implicate compression.

Another $3x3$ matrix, the initial cell basis vectors, give vectors with positions of the wall surrounding the sample, referred to as the boundary.

Periodic boundary conditions (PBC) are implemented in the version of LS-DEM used in this thesis. The principles of such boundary conditions are described in (W. Yang et al., 2014) and briefly presented here. PBC involve that whenever a particle moves out of one periodic boundary, it can be considered a part of another periodic boundary. For a rectangular prism the top is connected to the bottom while correspondingly, the right side is coupled to the left. Should a particle move out from the bottom, it will reappear at the top. When particle 1 and 3 (Figure 4.1) exceeds PB1, forces due to interactions with particles near PB2 are taken into account. When the center of a particle ($1'$ or $3'$) crosses PB2, it moves to a new position while dynamic parameters remain identical. Implementing the boundary conditions as periodic is advantageous because it does not require a particle-boundary interaction algorithm.

A library of 78 representative grains have been used in order to build the sample. Each grain has its own morphology file containing information on the volume of the grain and its moment of inertia, as well as the mass center of the level set. Further, the file gives the number of points discretizing the surface of the grain, the coordinates of each point, radius of a bounding box surrounding the particle, level set dimensions and lastly the level set values. Accordingly, all the grains vary in both size and shape.
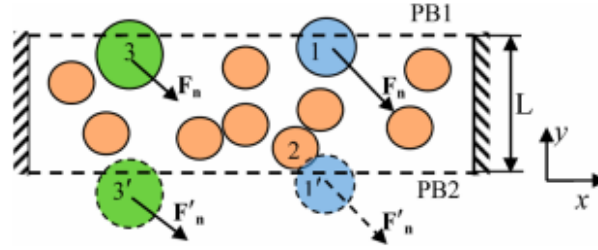
Figure 4.1: Illustration of periodic boundary conditions (W. Yang et al., 2014).

The size of the cubic sample is defined by choosing an amount of grains, n, that is assumed equal in all three dimensions. Then n^3 grains, which will constitute the sample, are randomly selected from the library of the representative grains, and their respective identities are stored in a morphology file. Grain properties, such as the density of particles, normal and shear stiffness in grain-to-grain contact and the coefficient of interparticle friction, are stored and can be modified in a properties file.

The randomly selected grains are assembled in a gas-like "cloud" with initially no contact. Further, the grains are packed at the strain rate defined in the applied strain rate matrix until the desired void ratio is reached. The corresponding obtained initial fabric is visualized in Figure 2.2b. When target void ratio is reached, there should be no overlapping of grains and no initial stresses. The packing stage is therefore concluded with a relaxation phase, where the grains regain their stiffness, stresses are reset to approximately zero and the big particle overlaps are removed.

The second phase simulates consolidation of the sample built in the previous stage. In this phase, the sample is compressed to a specified pressure level. This is done by applying pressure to the normal planes, i.e. specifying pressure level on the diagonal entries of the applied stress matrix. The compression can be performed either isotropically or anisotropically, by varying the the pressures applied on the normal planes.

The shear phase can be run in several different ways. By modifying the code and boundary conditions, tests like drained and undrained triaxial compression and extension tests can be simulated. It is also possible to simulate cyclic tests.

The size of the time step may be adjusted in order to avoid stability issues. Global damping is implemented in the current version of LS-DEM.

4.2   Running the Simulations

In the following sections, the simulation procedures performed to obtain the results in this thesis are presented.

The simulation routine has to be run through a Linux terminal. To get familiar with the code and the Linux shell, several analyses were run with a smaller sample (4^3 and 6^3 grains) on our personal computers before the analyses presented in this thesis were started. The bigger simulations, which are presented in this thesis, were run on a commercial cluster with support from NGI.
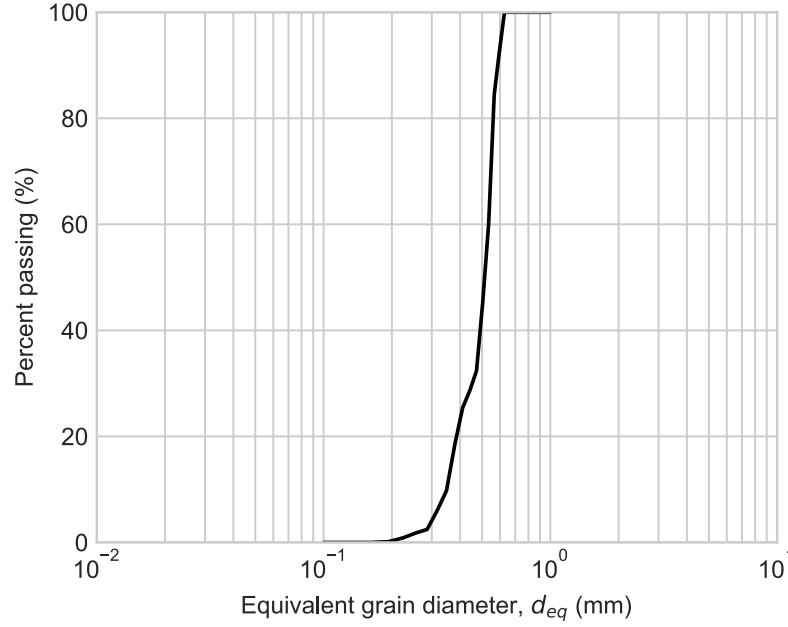
Figure 4.2: Particle size distribution of the sample.

4.3   Sample Preparation

Striving to avoid strain localization, a small number of grains have been simulated. This was also an important measure to keep the computational cost at an acceptable level.

A cubic sample consisting of 16 grains in each direction was used to calibrate the SANISAND input parameters. $16^3 = 4096$ grains were selected from the library, and packed at a strain rate of 5% on the normal planes until the desired target void ratios of 0.6, 0.65, 0.8 and 1.0 were reached. Global damping, with a damping coefficient set to 5000, is used in all three simulation phases to retain a quasi-static solution.

The particle size distribution of the sample is plotted for the equivalent grain diameter (4.1), and given in Figure 4.2. However, since only the equivalent grain diameter is used, this curve will likely look slightly different from a grain size distribution curve for the same material obtained in the lab. This is due to the physical nature of the sieving procedure, where each grain is characterized by the size of its longest axis not passing through the sieve.

$$d_{eq} = 2 \left(\frac{3V}{4\pi} \right)^{1/3} \tag{4.1}$$

The physical input parameters are given in Table 4.1, and taken from (Kawamoto et al., 2018). It is remarked here that their density value does not match corresponding values for natural soils. The matter is further discussed in Section 7.1.

Further, the samples were isotropically compressed to different pressure levels, giving the initial conditions summarized in Table 4.2. The initial conditions were chosen to represent the range of stresses

Table 4.1: Physical input parameters for the DEM simulations.

Particle parameters	Value	Unit
Density	23522	g/m^3
Normal stiffness	30000	N/m
Shear stiffness	27000	N/m
Friction coefficient	0.50	-

typical for geotechnical engineering. Moreover, going to higher stresses would bring the simulations into a domain where crushing of grains gets significant, which is outside the scope of this thesis.

Table 4.2: Simulated initial conditions.

| Void ratio before consolidation	Void ratio after consolidation	Cell pressure
0.6	0.5949	$10\ kPa$
0.6	0.5911	$100\ kPa$
0.6	0.5620	$1000\ kPa$
0.65	0.6336	$100\ kPa$
0.8	0.7635	$10\ kPa$
0.8	0.7622	$100\ kPa$
0.8	0.7478	$500\ kPa$
0.8	0.7134	$1000\ kPa$
1.0	0.8210	$10\ kPa$
1.0	0.8259	$100\ kPa$
1.0	0.8092	$500\ kPa$
1.0	0.7714	$1000\ kPa$

By considering the strain levels in all three principal directions after it was compressed, it was determined that the material could be considered as isotropic. This conclusion was drawn due to the fact that the strain levels were almost identical in all three principal directions, in addition to negligible shear strain levels. Moreover, the preparation method used in this thesis is meant to give isotropic fabric.

4.4 Simulation Procedure

Simulations of drained triaxial compression tests with constant mean pressure, p, were conducted. A strain rate of 10% was imposed in the horizontal directions ($\dot{\varepsilon}_2$ and $\dot{\varepsilon}_3$), while a vertical stress, $\sigma_1 = 3p - \sigma_2 - \sigma_3$, was imposed to keep the mean pressure, p, constant (Figure 4.3a). To simulate undrained behavior, strain ratios $\dot{\varepsilon}_2 = \dot{\varepsilon}_3 = -0.5\dot{\varepsilon}_1$ were imposed to ensure zero volumetric strain. In our case, strain ratios $\dot{\varepsilon}_2 = \dot{\varepsilon}_3 = 0.05$ and $\dot{\varepsilon}_1 = -0.10$ were applied. A total of 4 000 000 - 5 000 000 time steps were necessary to reach critical state, resulting in a computational time of about 70-90 hours for each analysis. The undrained analyses were not run to critical state, which resulted in shorter computational time (about 40 hours). A smaller time step was used in these analyses to better capture the response at small strains.
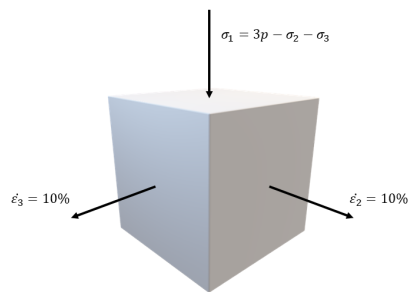
(a) triax pcst
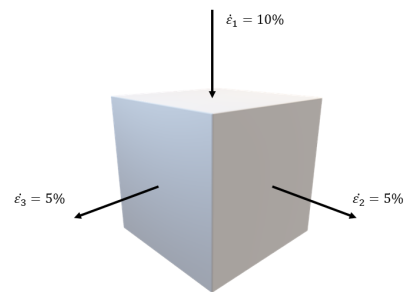
(b) triax undrained

Figure 4.3: Triaxial compression with constant mean pressure and undrained triaxial compression.

Chapter 5

Parameter Calibration

Simulations of drained triaxial compression tests with constant mean pressure, p, were used to calibrate most of the input parameters. The SANISAND input parameters are as given in Table 2.2. Initially, the CSL parameters and elastic stiffness parameters were determined. Since all plasticity parameters in the model are related to the CSL, these were calibrated subsequent to fixing the CSL. First of these, the bounding surface and dilatancy surface constants were calibrated. Following were the plastic hardening parameters. Lastly, the dilatancy parameter was set. The critical state parameters, bounding surface constant and dilatancy constant were calibrated using the Python routine given in Appendix A.

The analyses used to calibrate the SANISAND model are stated in Table 5.1.

Table 5.1: Analyses simulated to calibrate the SANISAND input parameters.

Name	Type of analysis	Void ratio before consolidation	Consolidation pressure
DEM1	triax pcst	0.6	$10\ kPa$
DEM2	triax pcst	0.6	$100\ kPa$
DEM3	triax pcst	0.6	$1000\ kPa$
DEM4	triax pcst	0.8	$10\ kPa$
DEM5	triax pcst	0.8	$100\ kPa$
DEM6	triax pcst	0.8	$500\ kPa$
DEM7	triax pcst	0.8	$1000\ kPa$
DEM8	triax pcst	1.0	$10\ kPa$
DEM9	triax pcst	1.0	$100\ kPa$
DEM10	triax pcst	1.0	$500\ kPa$
DEM11	triax pcst	1.0	$1000\ kPa$
DEM12	triax undrained	0.6	$100\ kPa$
DEM13	triax undrained	0.6	$10\ kPa$
DEM14	triax undrained	0.65	$100\ kPa$
DEM15	triax pcst	0.65	$100\ kPa$

Since crushing of grains is not considered in this thesis, the LCC parameters are not calibrated. This is also the case for the extension parameter, c. Further, the constants z_{max} and c_z address fabric change effects under cyclic loading, and are therefore not incorporated in this calibration.

5.1 Elasticity Parameters

The initial shear stiffness, G_0, as well as the initial bulk modulus, K_0, was found by assessing the stiffness at very small strains, assumed to represent elastic behavior. This part of the simulations is visualized in 5.1. The size of the time step was reduced in order to ensure a stable solution.
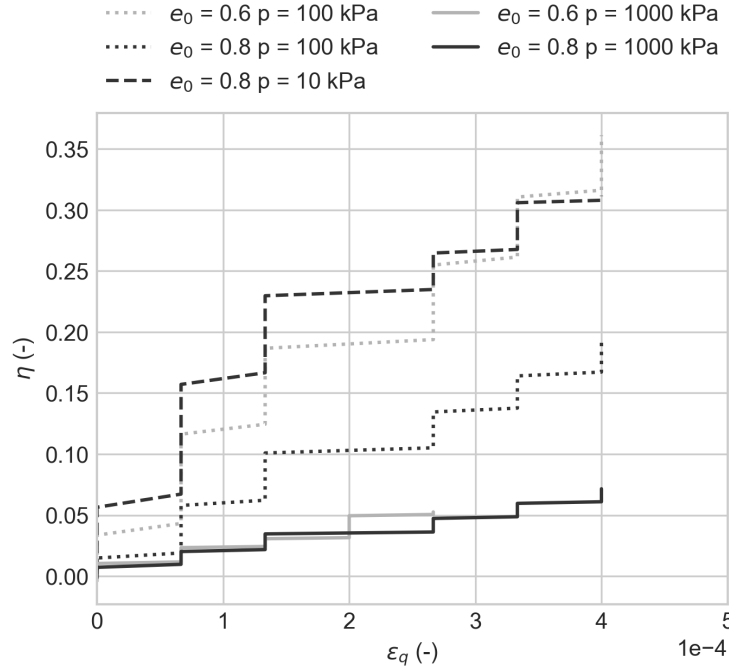

Figure 5.1: Initial phases of triaxial test to assess initial shear stiffness.

The elastic shear modulus is proportional to the ratio of change in deviatoric stress and strain, and was found between each data point from the analyses according to Equation (5.1).

$$G = \frac{\dot{q}}{3\dot{\varepsilon}_q^e} \tag{5.1}$$

Subsequently, G_0 was found by the use of the relation given in Equation (5.2) for every calculated G, derived from Equation (2.21). The final G_0 for each analysis was set as the average of the G_0-values.

$$G_0 = \frac{G}{p_{at}} \frac{(1+e)}{(2.97-e)^2} \left(\frac{p_{at}}{p}\right)^{1/2} \tag{5.2}$$

Table 5.2 gives the analyses used to calculate the respective G_0's. The average of the obtained values for every analysis, was used as the final G_0. It was calculated to be 58.1, and is for simplicity set to $G_0 = 60$.

Further, the elastic bulk modulus, K, was found by combining Equation (2.10) and (2.11) so it yields as in Equation (2.22). K was calculated by assuming a constant Poisson's ratio equal to 0.05.

$$K = \frac{\dot{p}}{\dot{\varepsilon}_v^e} \tag{5.3}$$

Table 5.2: Analyses used to calibrate G_0.

Name	Void ratio before consolidation	Cell pressure	G_0
DEM2	0.6	$100 kPa$	86.6
DEM3	0.6	$1000 kPa$	55.8
DEM4	0.8	$10 kPa$	29.7
DEM5	0.8	$100 kPa$	56.1
DEM7	0.8	$1000 kPa$	62.1

Then the relation yielding K_0 (5.4) was derived from (2.22). K_0 was, based on the average value, set to be $K_0 = 175$.

$$K_0 = \frac{K}{p_{at}} \frac{e}{1+e} (\frac{p_{at}}{p})^{2/3}$$

(5.4)

5.2 Critical State Parameters

The results from the LS-DEM analyses DEM1-DEM11 were used to calibrate the CSL (Table 5.1). Figure 5.2 and shows that all 11 analyses reached a well defined critical state, indicated by a state where strains are applied without change in either stress ratio, $\eta = q/p$ nor void ratio, e.
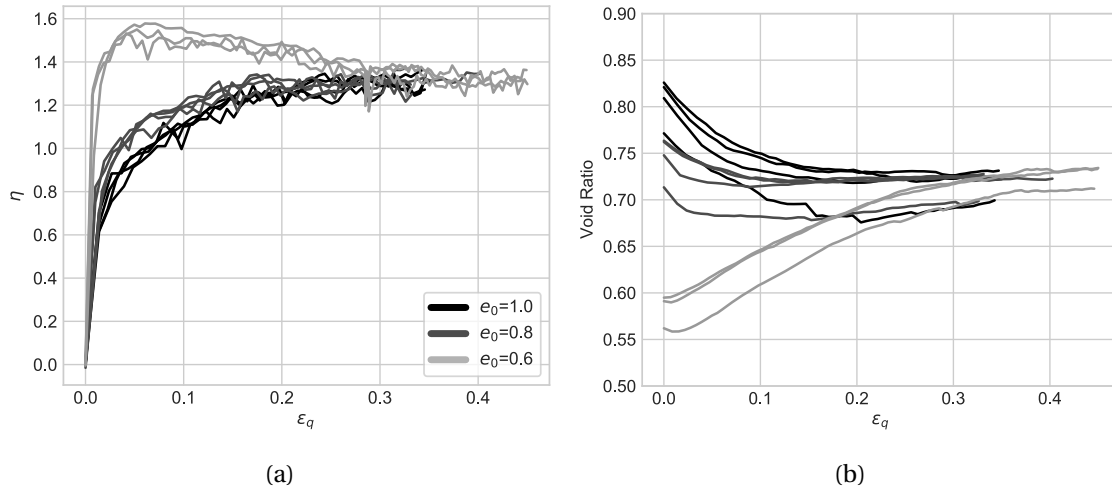
Figure 5.2: (a) Stress plot for DEM1-DEM11. The curves flatten out at approximately $\eta = 1.35$, which indicates a well defined critical state. (b) $\varepsilon_q - e$ plots for DEM1-DEM11.

The stress paths in the $p - q$ space for each analysis were plotted, and $M = (q/p)_{critical} = 1.35$ was found as the slope of the q_c-line fitted to the end point of each stress path (Figure 5.3). By assuming a small $m = 0.01$, the value of α^c was set to $\alpha^c = M - m \approx 1.35$.

Similarly, e_{c0}, λ_c and ξ were determined by fitting the e_c-curve (2.23) to the $p - e$ stress paths (Figure 5.4). The obtained CS parameters are summarized in Table 5.3. The curve fitting was done by linear regression of e_c versus $(p/p_{atm})^{\xi}$ after $\xi = 0.4$ was set by trial and error.

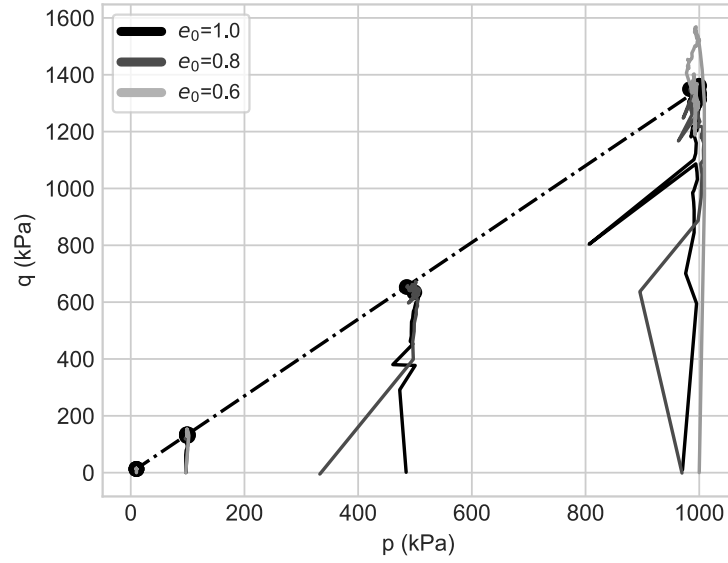Figure 5.3: Critical stress ratio, $(q/p)_c = 1.35$. The observed jumps in stresses is due to numerical issues, which is discussed in Section 7.3.
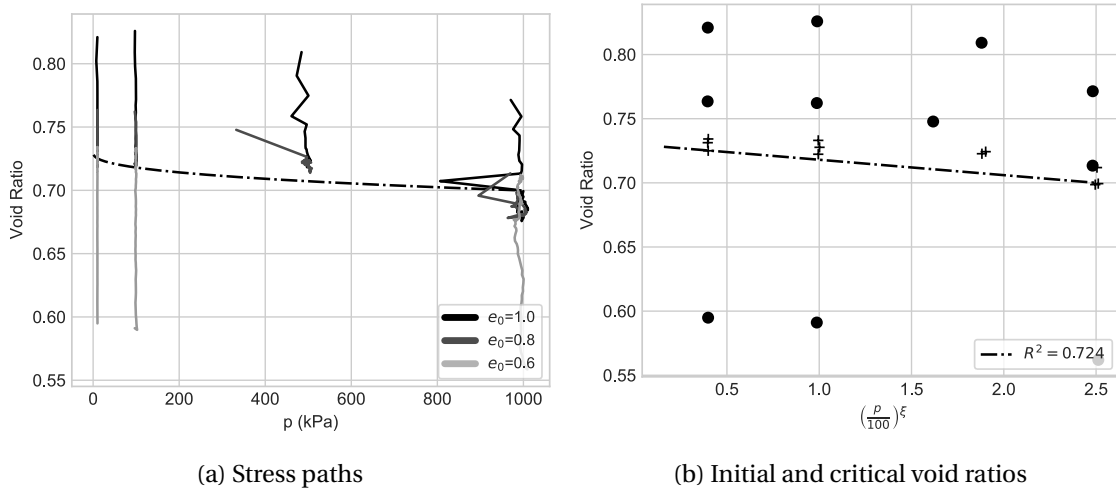

(a) Stress paths

(b) Initial and critical void ratios

Figure 5.4: Calibration of CSL constants using the results from LS-DEM analyses DEM1-DEM10.

Table 5.3: CSL parameters.

Parameter	Value
α_c	1.35
e_{c0}	0.73
λ_c	0.012
ξ	0.4

5.3   Bounding Surface and Phase Transformation Line

The bounding surface constant, n^b, was found by evaluating results of the analyses run from dense state. Rearranging Equation (2.25) at peak stress ratio, gives Equation (5.5).

$$n^b = \frac{1}{\psi^b} \ln\left(\frac{\alpha^c}{\alpha^b}\right) \tag{5.5}$$

Where ψ^b and α^b are the values of ψ and α (or η) at the peak stress-ratio state. Further, the peak stress ratios and corresponding state parameters were extracted from the results, and plotted in the $\psi - \ln(\frac{\alpha^c}{\alpha^b})$ space. Since $\psi = 0$ refers to critical state, $\ln(\frac{\alpha^c}{\alpha^b})$ is equal to 0 for $\psi = 0$.

By the use of linear regression, the bounding surface parameter $n^b = 1.3$ was found (Figure 5.5).

(a)   (b)
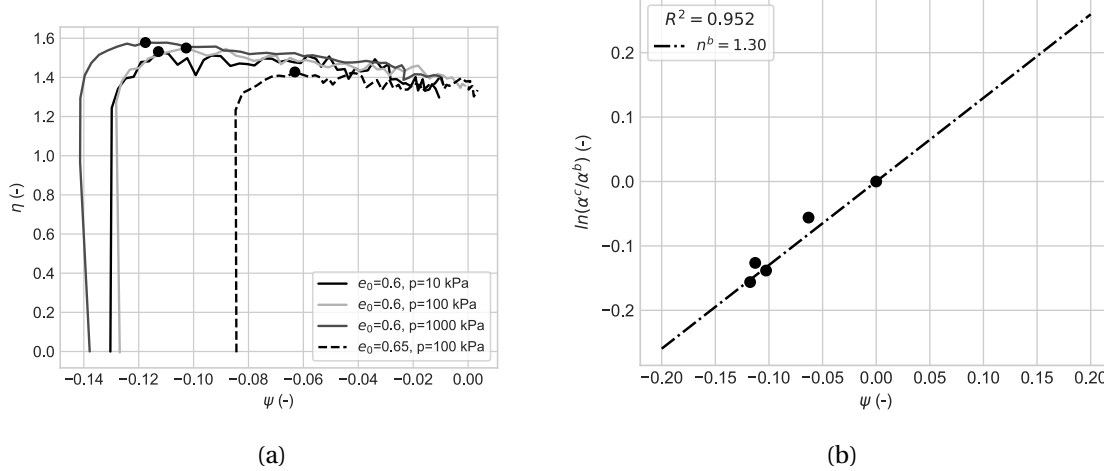
Figure 5.5: Calibration of n^b using the results from DEM1-DEM3 and DEM15.

Simulations of undrained triaxial analyses were used to calibrate the slope of the phase transformation line, n^d (DEM12-DEM13). Similarly to the bounding surface parameter, n^d was obtained by plotting $\ln(\frac{\alpha^d}{\alpha^c})$ versus ψ^d, where α^d and ψ^d refers to α and ψ at phase transformation state (Figure 5.6). The slope of the line was found to be 1.94 by linear regression. Due to the uncertainty of the value, $n^d = 2$ is used in the rest of this thesis for simplicity.

Figure 5.6: Calibration of the phase transformation line, n^d, from simulations of undrained tests.

5.4 Kinematic Hardening Parameters

Kinematic hardening parameters, c_h and h_0, were estimated by trial and error in PLAXIS Soil Test. In the Soil Test interface, the initial stresses were adjusted in order to make them correspond to the level of isot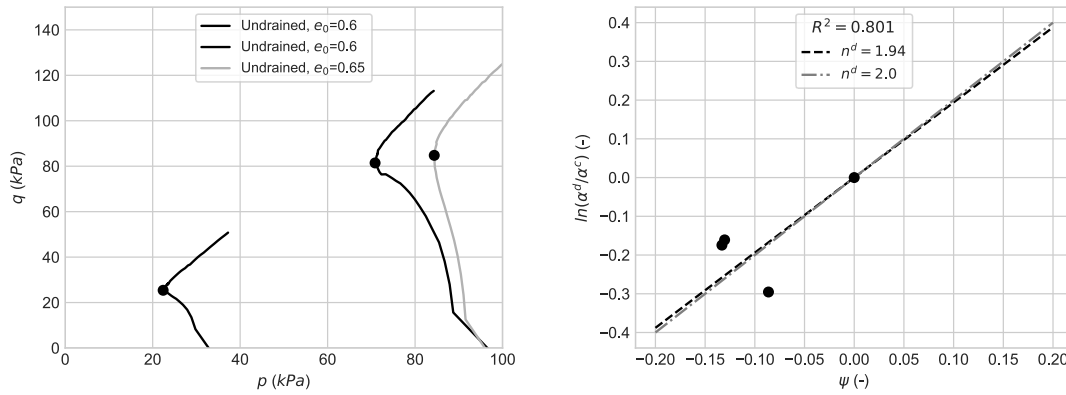ropic consolidation in the respective LS-DEM analyses. In addition, the boundary conditions were chosen as stress increments in order to keep the mean pressure constant. For all soil tests the drainage condition was specified to be drained.

The analyses stated in Table 5.4 were assumed a representative selection of the simulations run, and were used for the estimation.

Table 5.4: Analyses used to calibrate h_0, c_h and A_d.

Name	Void ratio before consolidation	Cell pressure
DEM2	0.6	100 kPa
DEM7	0.8	1000 kPa
DEM9	1.0	100 kPa
DEM15	0.65	100 kPa

Specifically, the hardening parameter, h_0, was found by fitting the curves from Soil Test of the stress ratio $\eta = q/p$ plotted against the deviatoric strain with the corresponding LS-DEM simulations. By initially assuming $c_h = 0.97$ and varying h_0, it was observed that the best fit was obtained for $h_0 = 6$ (Figure 5.7).

Further comparisons of this value with different c_h-values, showed that $c_h = 1.1$ gave the best fit for all analyses in Table 5.4. LS-DEM simulations plotted against results obtained from Soil Test in PLAXIS with hardening parameters, $h_0 = 6$ and $c_h = 1.1$, are given in Figure 5.8. These parameters were find prior to A_d. Accordingly A_d was, for the calibration of kinematic hardening parameters, preliminary set to be zero. Therefore, as seen in Figure 5.7 and 5.8, the softening post peak behavior for the densely packed samples is not captured by SANISAND.
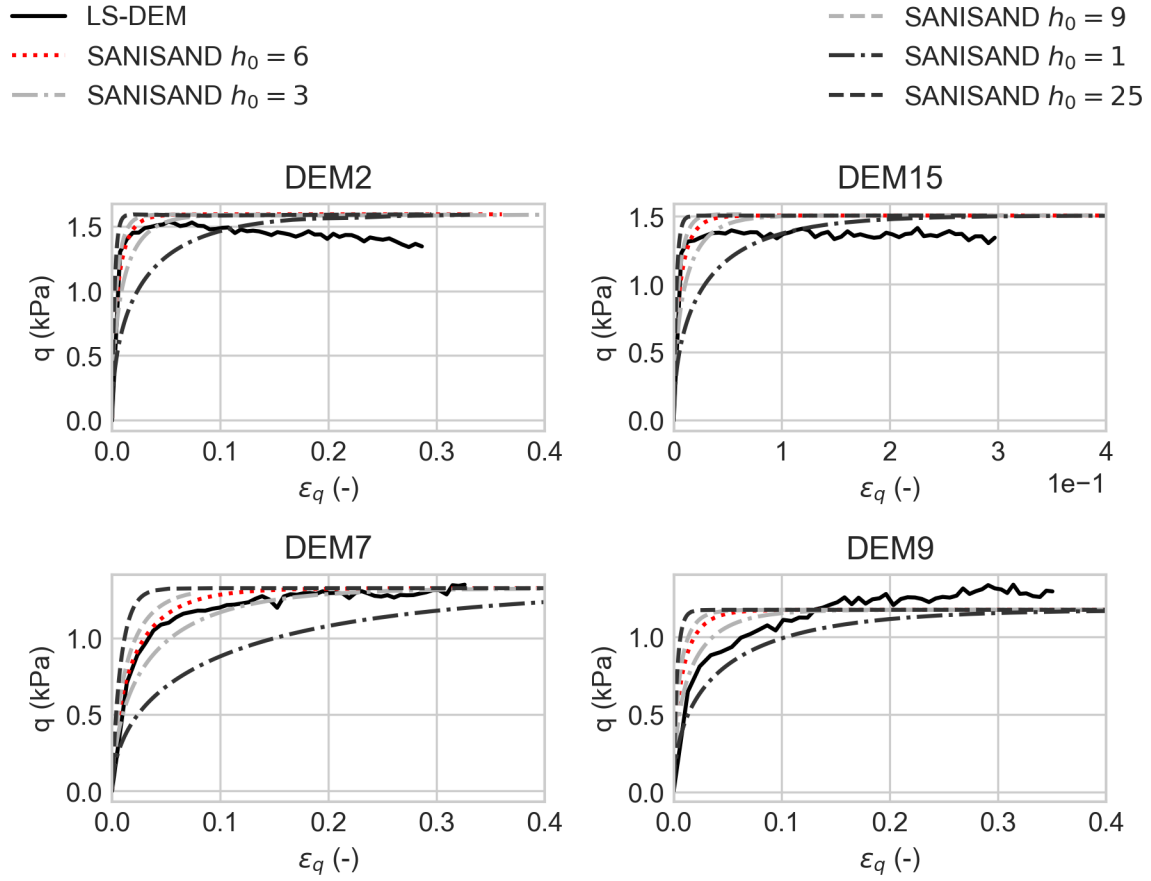
Figure 5.7: LS-DEM results compared with curves from PLAXIS Soil Test with different h_0-values.
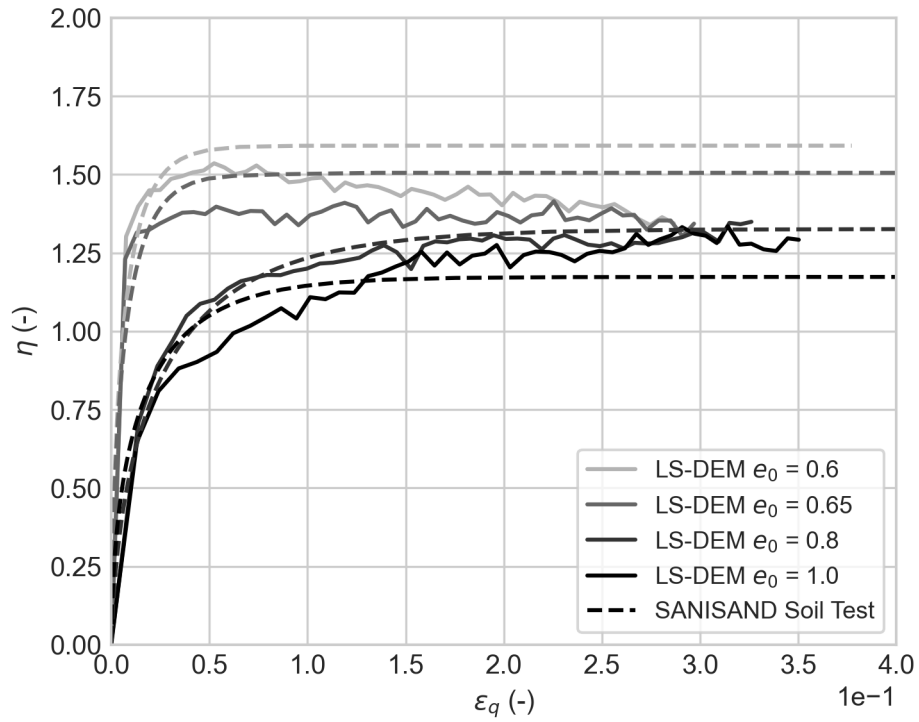
Figure 5.8: LS-DEM versus curves from PLAXIS Soil Test with $h_0 = 6$ and $c_h = 1.1$.

Dilatancy Parameter, A_d

When ignoring small elastic deformations in drained tests, the following approximation and relation yields:

$$\frac{\dot{\varepsilon}_v}{\dot{\varepsilon}_q} \approx \frac{\dot{\varepsilon}_v^p}{\dot{\varepsilon}_q^p} = A_d(\alpha^d - \alpha) \tag{5.6}$$

From this, the dilatancy parameter, A_d, was estimated with trial and error based on $\varepsilon_V - \varepsilon_q$ curves. The analyses stated in Table 5.4 were used. A good fit to the volumetric strain - deviatoric strain was obtained with $A_d = 1.1$, as can be seen in Figure 5.9.
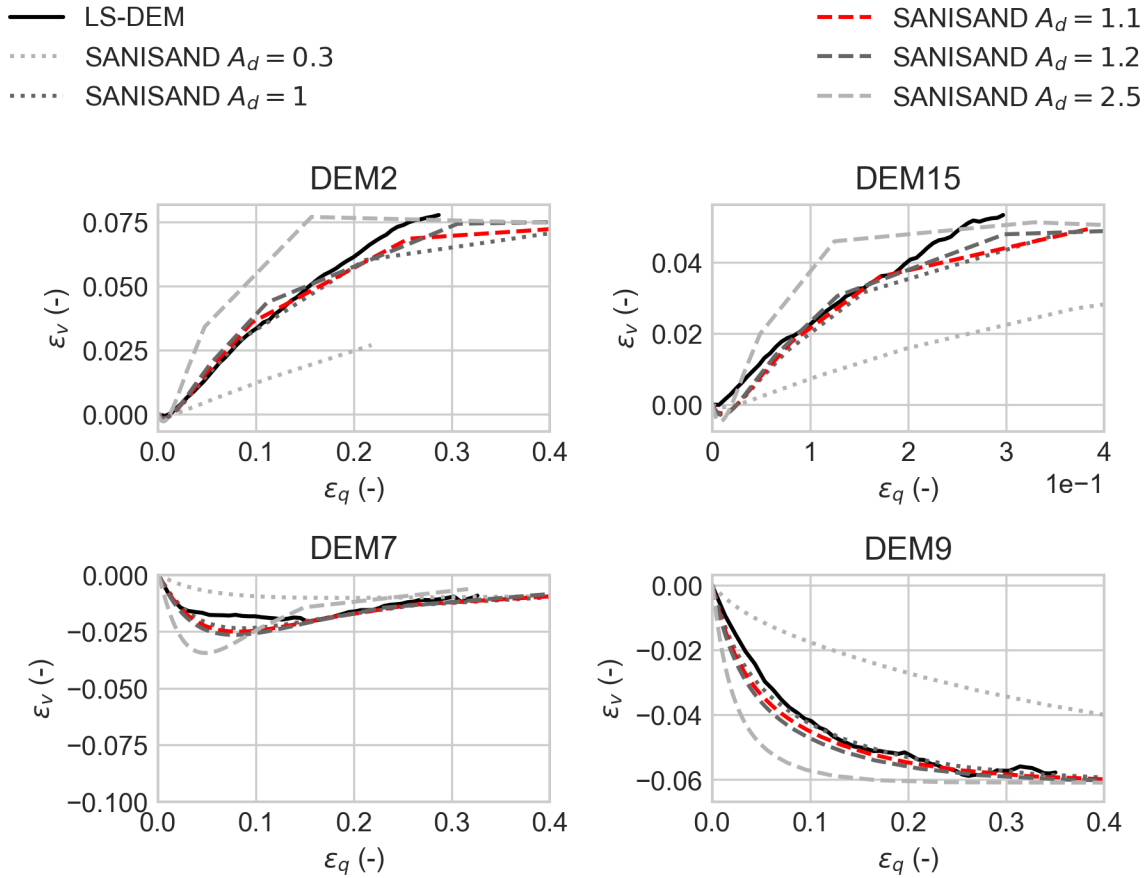
Figure 5.9: LS-DEM versus curves from PLAXIS Soil Test with different A_d-values.

5.5 Results

Figure 5.10 and 5.11 show a comparison of the results obtained from the LS-DEM simulations and the response from SANISAND with all the calibrated input parameters in Table 5.5.

Table 5.5: Calibrated input parameters for the SANISAND model.

	Parameter	Hostun Sand
Elasticity	G_0	60
	K_0	175
CSL	α_c^c	1.35
	c	-
	e_0	0.73
	λ	0.012
	ξ	0.4
Yield Surface	m	0.01
Dilatancy	n^d	2.0
	A_d	1.1
Kinematic hardening	n^b	1.3
	h_0	6.0
	c_h	1.1
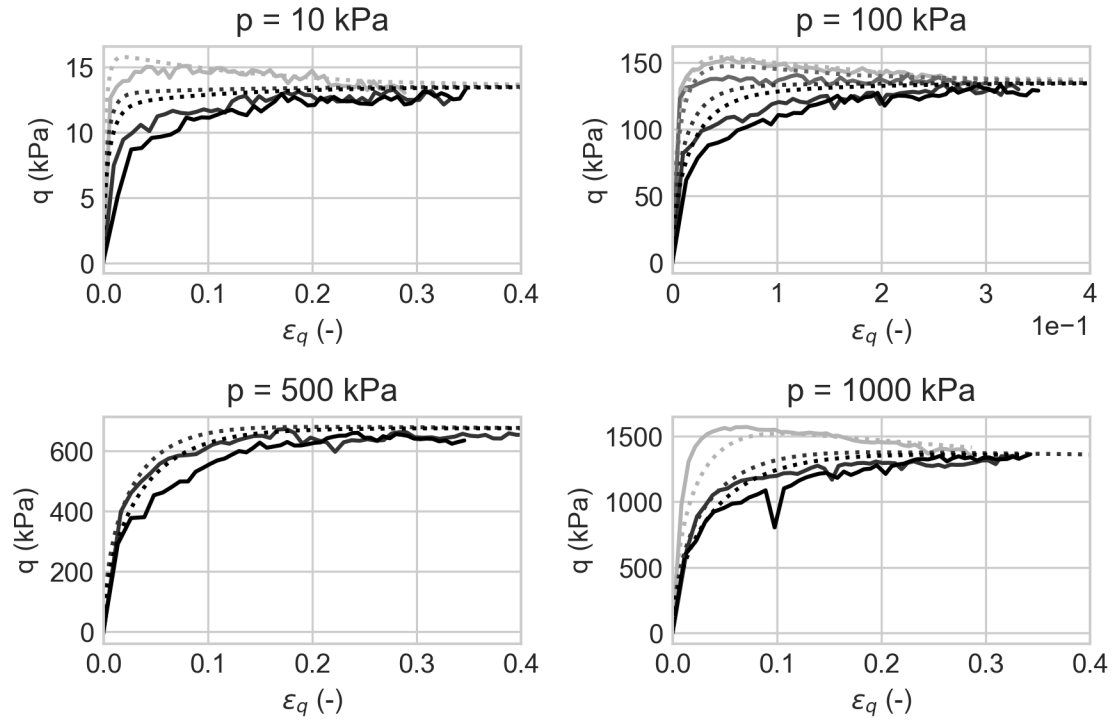
Figure 5.10: Comparison of LS-DEM results with SANISAND.
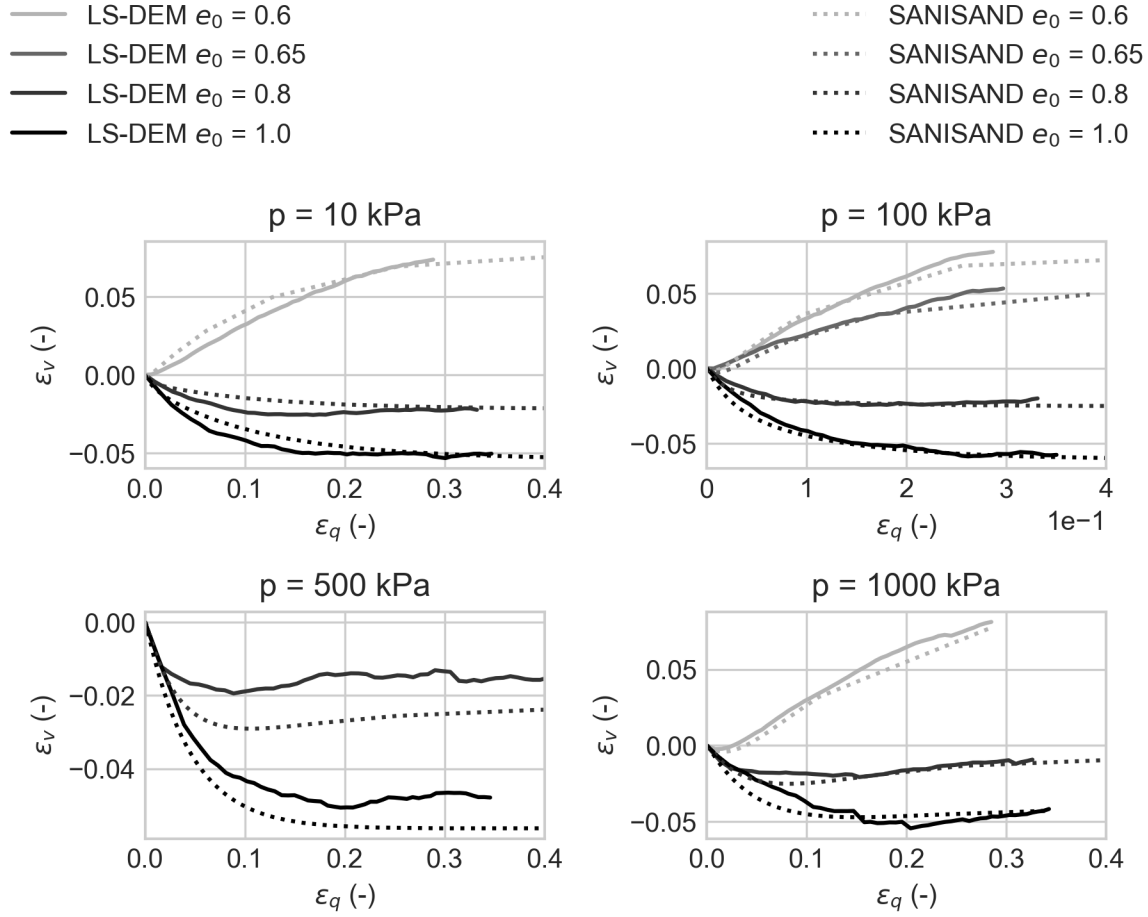
Figure 5.11: Comparison of LS-DEM results with SANISAND.

5.6 Evaluation of Calibration

To evaluate the calibrated input parameters, the SANISAND response was compared with LS-DEM results for another stress path than the constant mean pressure path. Such a comparison was performed by simulating regular strain-controlled triaxial compression tests with LS-DEM. The boundary conditions for TEST1-TEST2 are visualized in Figure 5.12. Similar conditions were recreated in the Soil Test interface by applying vertical stresses. Constant stress in the horizontal directions was ensured by adjusting the stress increments in these directions to be zero.

Table 5.6: Analyses used to evaluate the obtained SANISAND input parameters.

Name	Type of analysis	Void ratio before consolidation	Consolidation pressure
TEST1	triax strain	1.0	100 kPa
TEST2	triax strain	0.65	100 kPa
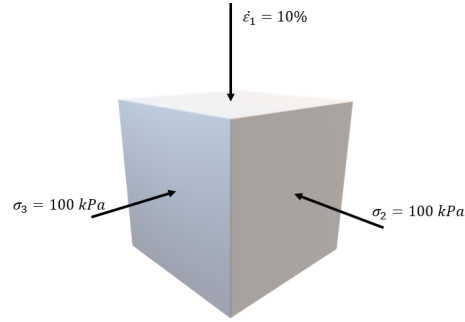
Figure 5.12: Boundary conditions for TEST1-TEST2.
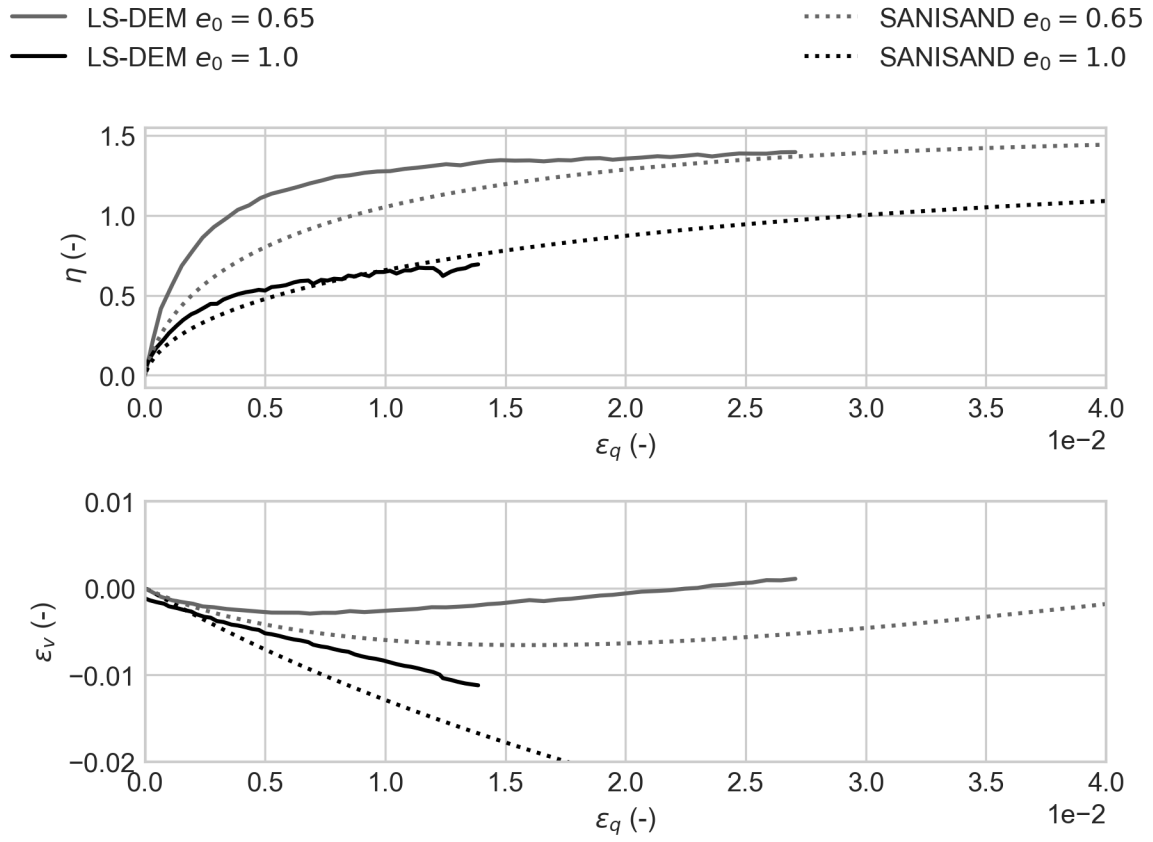
Figure 5.13: Evaluation of calibrated SANISAND input parameters by comparing them with strain-controlled triaxial LS-DEM simulations.
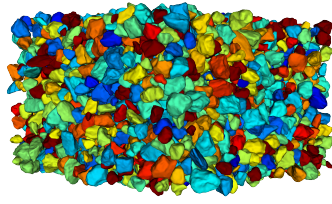
(a) DEM4
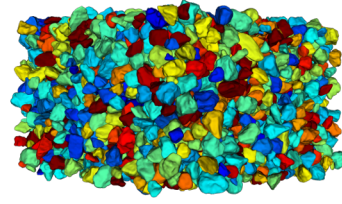
(b) DEM5
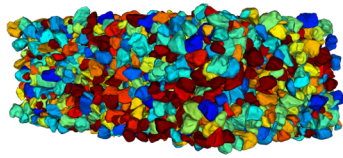
(c) DEM6
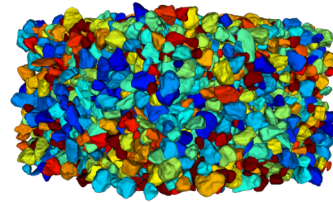
(d) DEM7

Figure 5.14: Visualization of sheared samples, with initial void ratio $e_0 = 0.8$ and average pressures $p = 10, 100, 500$ and $1000\,kPa$.

Further evaluation of the LS-DEM simulations was done by visually studying the grain kinematics after the analyses. By the use of a LS-DEM grain visualization program, the grains were plotted with correct position and rotation at the end of each analysis, with colors representing the magnitude of the rotation. The visualization program was run on a Linux server provided by NGI, and used the LS-DEM results as input parameters.

The following was observed:

- No development of shear bands in the samples.

- The deformation of the samples looks homogeneous.

- Large rotation of grains seems to appear completely random in the sample. This may be a consequence of the number of grains "floating" in the sample, hence not interacting with any other grains. This matter is investigated further in Section 7.3.

- DEM6 is significantly more compressed than the other samples. It is also in this simulation the most significant jump in stresses is observed, which indicates numerical instabilities.

Chapter 6

The Effect of Grain Shape in Critical State

6.1 Methodology

To investigate to what extent grain shape affects the critical state line, the grains in four of the analyses were replaced with spherical grains. This was done by the use of level set-functions of spherical grains with the same volume as the real grains. These grains were packed to the same initial void ratio and isotropically compressed to the same cell pressure as the previous simulations. The following initial conditions were then obtained (Table 6.1):

Table 6.1: Initial conditions simulated with spherical grains.

Void ratio before consolidation	Void ratio after consolidation	Consolidation pressure
0.6	0.5858	$100\ kPa$
1.0	0.7183	$10\ kPa$
1.0	0.7208	$100\ kPa$
1.0	0.6607	$1000\ kPa$

The CSL parameters were calibrated with the same approach as described in the previous chapter.

6.2 Results

The same exponent for stress dependency, $\xi = 0.4$, was used for the spherical grains to visually compare the two parameter sets. The rest of the calibrated critical state parameters are given i Table 6.2, together with the corresponding parameters for Hostun sand. Further, they are plotted in Figure 6.1 and 6.2.

Table 6.2: CS parameters for spherical grains.

Parameter	Hostun sand	Spheres
α_c	1.35	0.93
e_{c0}	0.74	0.65
λ_c	0.012	0.019
ξ	0.4	0.4
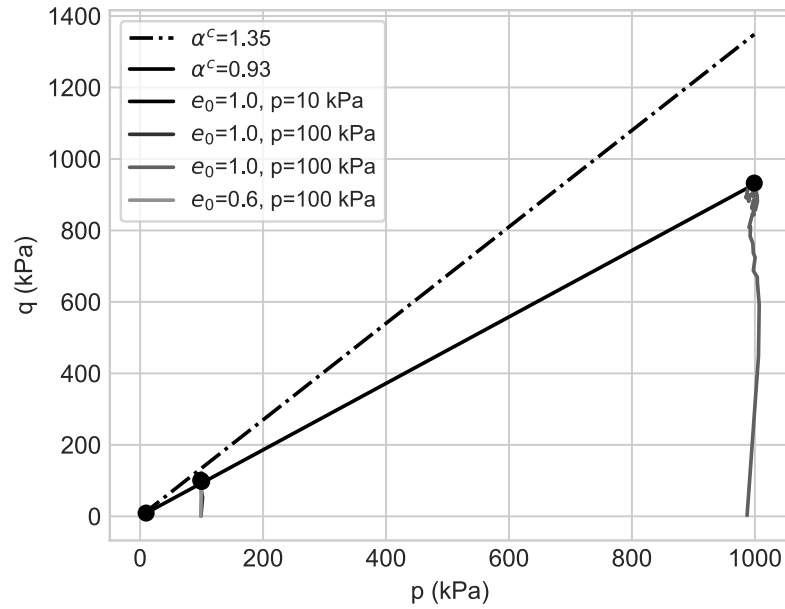
Figure 6.1: Critical stress ratio for spheres compared to Hostun sand.
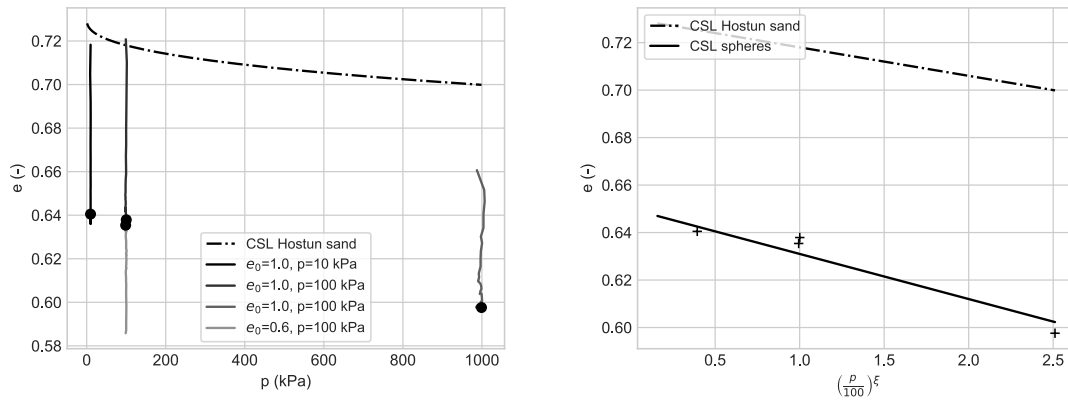

Figure 6.2: Critical state line calibrated for spheres compared to Hostun sand.

The following is observed from the plots:

- The critical stress ratio is considerably lower for the spherical grains.

- The critical void ratio is lower for spheres than Hostun sand.

- In this calibration, the critical void ratio for spheres is slightly more pressure dependent than it is for Hostun sand.

Chapter 7

Discussion

7.1 Calibration of SANISAND input parameters

Sample Preparation

When the grains of a soil sample have shapes other than spheres, not only the void ratio, but also the particle orientation will be decisive for the mechanical behavior. In this study, the grains are randomly placed in a "cloud" and pushed together until they reach contact and desired cell pressure. This method obviously deviates from how sand grains are deposited in the nature, where gravitational forces are decisive for how the grains align relative to each other and the bedding. In addition, this packing method differs from how samples are prepared in the laboratory. This makes the numerical results less comparable to experimental data. Another important observation is that natural sands often are anisotropic, while that is not the case for this investigated sample. This may also impact the calibrated parameters. On the other side, all simulations were run with the exact same collection of grains, which eliminated the issue of sample variation.

The grain density used in the simulations was set to be $7.53 \cdot 10^{-11} g/vox$. With $1\,pix = 1.4741 \cdot 10^{-5}\,m$, the density is $\rho_s = 23522\,g/m^3$. This does not coincide with a natural soil, which typically has density in the range of $2500\,kg/m^3$. However, this is only a numerical value of which the investigated results are independent. Hence, this is not of importance to the simulations run in this thesis, and will not affect the calibrated results. The grain density will only affect the time step used in the calculation, which is a function of grain stiffness and mass. Hence, the simulations performed in this study have presumably been unnecessarily time consuming. Readers are asked to be aware of this error.

Elasticity Parameters

As it appears in Table 5.2 the calculated G_0-values vary from $29.7\,kPa$ to $86.6\,kPa$, even though these values are expected to be consistent for one type of sand. The discrepancies may be explained by numerical instabilities. An even smaller time step should have been applied in order to investigate whether this would result in a more consistent, and thereby accurate initial shear stiffness.

The average initial shear stiffness, G_0, was calculated to be 60, which is low compared to the corre-

sponding values for real sands. This observation coincides with the findings of Jostad et al. (2021). They also observe, based on both triaxial and oedometric simulations, that LS-DEM underestimate the elastic stiffness of the soil. This may be explained by the choice of stiffness contact model implemented in LS-DEM, which is further discussed in Section 7.4.

G_0 is generally higher for real sands and usually found experimentally by the use of dynamic analyses. Salvatore et al. (2018) adopts a set of parameters for Hostun sand, where $G_0 = 200$, while Chian et al. (2014) uses $G_0 = 150$ for their numerical analyses of Hostun sand.

Critical State Parameters

By examining the visualization of the sheared samples, it was concluded that the samples deforms without strain localizing in narrow areas. Hence, our hypothesis that a small cubic sample would help overcome the issue of strain localization, is assumed correct. Furthermore, LS-DEM enables running the analyses to large strains, and all analyses reached a well defined critical state.

Despite some numerical issues, the SANISAND equations capture the critical void ratios of the different analyses in a good manner. Following this, the void ratio is considered unique for a given mean pressure. However, the critical void ratio appears almost identical for mean pressures $p = 10 - 500 kPa$ before it does a negative leap at $p = 1000 kPa$. This behavior was not possible to capture with the SANISAND equations, which require a constantly decreasing critical void ratio for increasing mean pressure. Further, most literature shows decreasing e_c with increasing p, which indicates a possible issue with the LS-DEM analyses. Still, the calibration of the CSL is considered good, and close to unique.

In literature, different locations for the CSL are proposed for Hostun sand. Some of these deviate considerably from the suggested location proposed in this thesis. Salvatore et al. (2017) propose a CSL that is significantly more pressure dependent. However, the study performed by Salvatore involved tests on specimens exposed to large pressures where crushing of grains probably is significant. Further, the CSL in the study of Salvatore et al. is extrapolated to lower stresses, while the CSL proposed here is calibrated for low stresses. The CSL for Hostun sand referred to in (Zhao et al., 2021) is more similar to the CSL suggested in this study. Still, the scatter in obtained CSL parameters highlights the need for a more consistent calibration procedure.

DEM6 is observed in Figure 5.14c to be significantly more compressed vertically than the other samples. Investigation of the stress output from the consolidation phase reveals that the sample in fact was not isotropically compressed, but exposed to an anisotropic stress condition. Despite this, the sample did indeed reach the same critical void ratio as the other samples investigated, substantiating the existence of a unique critical void ratio for a given pressure.

The critical stress ratio, $M = q_c/p = 1.35$ was consistent for all analyses.

Bounding Surface and Phase Transformation Line

In the calibration of the bounding surface parameter, n^b (Figure 5.5), all analyses aligned, resulting in a well defined parameter. For n^d, however, the results were more scattered (Figure 5.6), making the slope of the line in the $\ln(\frac{\alpha^d}{\alpha^c}) - \psi^d$ space harder to determine. For a better calibration of this parameter, additional

initial void ratios should be simulated. This is also possibly due to an issue with the LS-DEM simulations, and should be investigated further.

Kinematic Hardening Parameters

The kinematic hardening parameters were calibrated using a trial and error procedure. h_0 was varied and found first, and then c_h was adjusted to optimize the fit. Even though the SANISAND responses correlate with the LS-DEM simulations, the fit is not completely accurate and discrepancies are especially observed for $e_0 > 0.6$. Generally, the SANISAND response behaves stiffer initially before it yields more abruptly than what is observed for the LS-DEM analyses. This is especially the case for the loosely packed samples.

Consequently, it was challenging to define the kinematic hardening parameters uniquely. The uncertainty of the kinematic hardening parameters may be attributed to the limited amount of analyses run from dense side. By increasing the amount of analyses, detecting patterns in the data could be easier while discrepancies in single analyses can more easily be eliminated. In addition, the time step size in the analyses of this study is too large to capture initial deformations pre peak. Decreased size of this may therefore contribute in more accurate calibration.

Dilatancy Parameter, A_d

Using a trial and error approach, a relatively good fit to the LS-DEM curves of volumetric strain plotted against deviatoric strain was obtained with $A_d = 1.1$. For the densely packed samples, SANISAND tend to underestimate the volumetric strains compared to LS-DEM. Further, the fit is particularly deviant for the analyses consolidated to $p = 500 kPa$. Despite these observations, the overall fit is considered reasonably good.

Calibration of SANISAND Input Parameters in PLAXIS Soil Test

Soil Test in PLAXIS, used for the trial and error calibration approach, enables easily adjusting input parameters to extract the SANISAND response with a certain, specific set of input parameters. Thereby, the effect of varying one input parameter can easily and efficiently be investigated by comparing the respective SANISAND responses.

However, a new Soil Test simulation is required for every new LS-DEM analysis, as a new analysis involves either a different void ratio or a new consolidation pressure. In addition, the adjustment of one parameter require a new simulation for every LS-DEM analysis. Consequently, the amount of analyses increase drastically with the amount of LS-DEM analysis to compare with, and the amount of parameters to calibrate and different values to be trialed. Even though one simulation in Soil Test rarely ran for more than five minutes, the approach easily becomes time consuming as the number of simulations needed is significant. Therefore, four analyses were considered representative for the entire selection of the LS-DEM analyses conducted and presented in this thesis. This measure considerably reducing the simulation time, but at the same time reducing the certainty of the parameter values set. Figure 7.1 summarizes the simulations performed in PLAXIS Soil Test, and illustrates how the procedure is prone to

be time consuming. Additionally, a trial and error approach involves varying more than one parameter, and it therefore makes it difficult to find a unique parameter set.
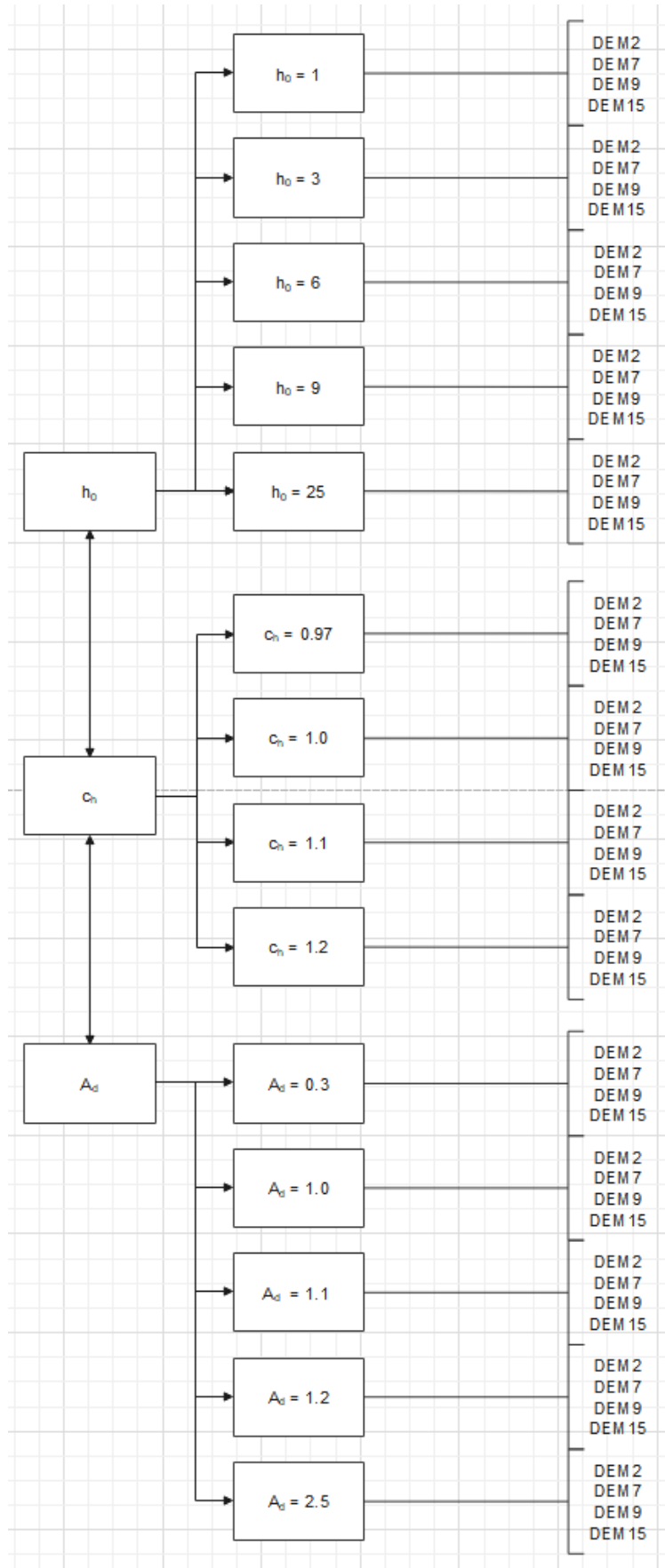
Figure 7.1: Trialed parameters in the calibration of h_0, c_h and A_d.

Python scripts were developed to graphically compare SANISAND Soil Test output with LS-DEM results. The comparison was done visually inspecting the plots, and then selecting the parameter value that gave the best fit. One adjustment could result in better fits initially, but greater discrepancies for larger strains. Therefore, selecting the best fit was a matter of assessment. There are accordingly uncertainties related to the parameters obtained using PLAXIS Soil Test.

Evaluation of Calibrated Parameters

DEM15 was, as opposed to the other analyses, not used for the calibration of CSL-parameters. DEM15 was therefore considered to be the best suited analysis for the evaluation. In addition, the shearing was performed as a regular strain-controlled triaxial compression test and not with constant mean pressure. These measures in an attempt to make the results for the evaluation independent from the results used in the calibration.

The evaluation performed yields promising results in the sense that the SANISAND response matches the results from the strain-controlled triaxial test. The analysis with $e_0 = 1.0$ fits, as anticipated, the SANISAND response more accurately. That is because this analysis has been used more for calibration purposes and hence it more extensively effects the obtained SANISAND model. It is further observed that for the strain-controlled triaxial tests, LS-DEM actually behaves stiffer than what SANISAND predicts. This further substantiates that the stiffness properties of LS-DEM are not consistent. These observations may indicate that the boundary conditions impact the stiffness properties obtained from LS-DEM.

Despite the fact that the strain-controlled triaxial analysis did match the SANISAND Soil Test response, the evaluation is limited and a validation should be performed. Ideally the evaluation should have been done with completely independent analyses, involving packing the samples to new void ratios and then compressing them to new pressures. This was not done due to time limitations.

7.2 The Effect of Grain Shape

Hostun sand was expected to reach a higher critical stress ratio than the collection of spheres. The irregularities of the angular Hostun grains give more friction and hence higher strength than what is observed with completely smooth grains. Further, Yang and Lou (2015) conclude that a lower overall regularity, as defined in Section 2.1, gives higher location of the critical state line. This coincides with the obtained results in this study. However, the stress dependency actually increases going from Hostun sand to spheres, which was unexpected.

Only four triaxial tests with spherical grains were simulated due to time limitations. However, since the two analyses run for $p = 100\,kPa$ reached the same critical void ratio, the uniqueness is expected to yield for other pressure levels as well.

7.3 Numerical Challenges in LS-DEM

Coordination Number

The term mean coordination number, Z, is defined as in Equation (7.1), and yields the average number of contacts per particle in a sample (Meng et al., 2014).

$$Z = 2\frac{N^C}{N} \tag{7.1}$$

Where N^C is the total number of contacts in the sample, and N the total number of grains. Figure 7.2a gives the evolution of coordination number during the triaxial phase for analyses DEM1-DEM10.

However, it is normal to use an updated coordination number, which considers only the grains in contact, as given i Equation (7.2).

$$Z_{updated} = 2\frac{N^C}{N - N_{rattlers}} \tag{7.2}$$

Where $N_{rattlers}$ indicates the number of grains not interacting with any other grains, so called rattlers. In numerical models, like LS-DEM, some rattlers are expected. In our samples, $15-39\%$ of the total grain volume was considered to be rattlers at CS, hence only $85-61\%$ of the grain mass in the samples was actually carrying load at critical state (Table 7.1).

Figure 7.2 gives the updated coordination number before and after the triaxial simulation, together with the corresponding number of rattlers.

Table 7.1: Number of rattlers before and after shearing, as well as the volumetric fraction of rattlers at critical state.

Analysis	Rattlers before shearing	Rattlers at CS	Fraction of rattlers at CS
DEM1	1894	1667	27 %
DEM2	2678	1791	34 %
DEM3	875	1085	15 %
DEM4	2901	1953	38 %
DEM5	2795	1917	36 %
DEM6	2726	1931	37 %
DEM7	2652	1818	35 %
DEM8	2940	1970	39 %
DEM9	2830	1943	38 %
DEM10	2752	1798	35 %

As expected, the number of contacts and hence coordination number decreases as the material is sheared towards critical state (Zhao et al., 2021). The flattening of the curve approaching critical state substantiates the findings of Thornton (2000), stating that the coordination number is constant at critical state. This coincides with the anisotropic critical state theory, as a constant fabric requires constant coordination number.

The number of rattlers is generally very high, which strongly affects the updated coordination num-
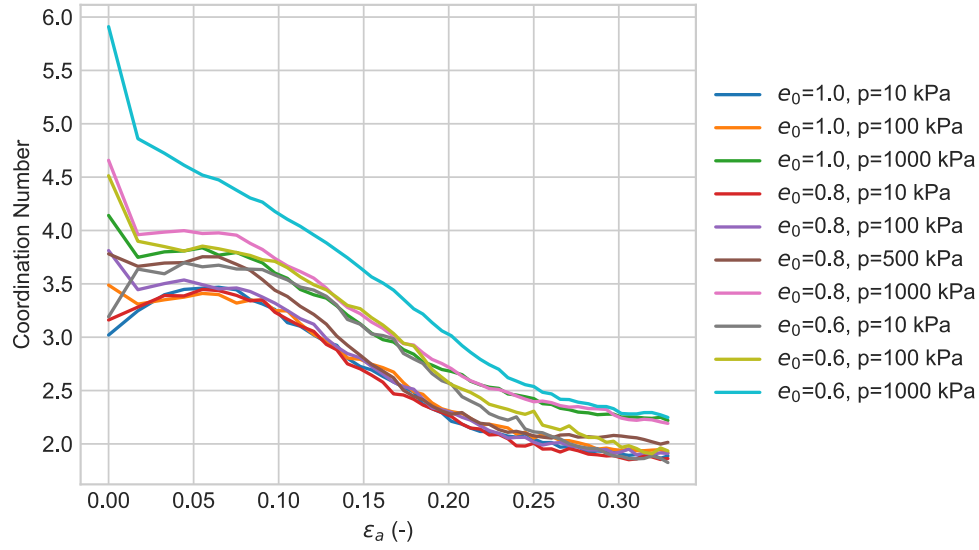
(a) Evolution of Coordination Number during the triaxial phase.
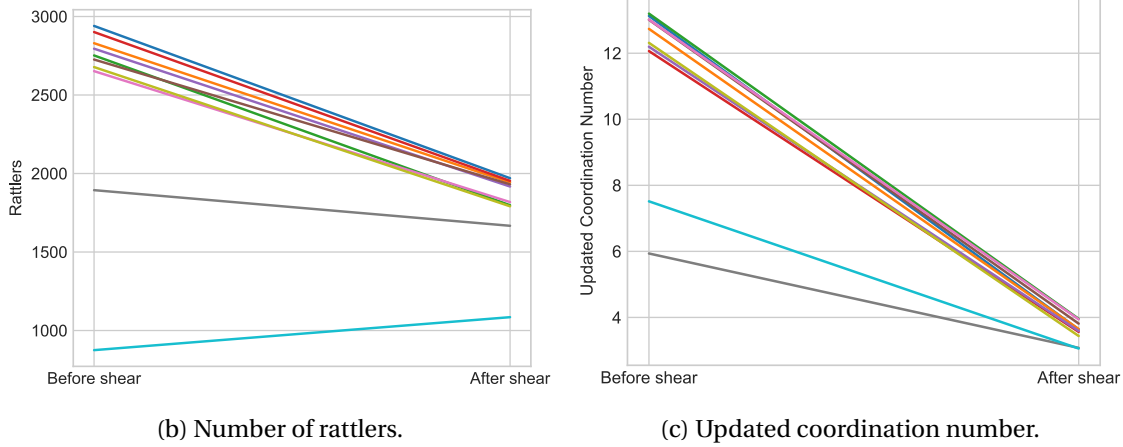
(b) Number of rattlers.

(c) Updated coordination number.

Figure 7.2: Number of rattlers and updated coordination number before and after the triaxial simulation.

ber. The number of rattlers in DEM1 and DEM3 deviates significantly from the other analyses. Since DEM2, which has the same initial void ratio as DEM1 and DEM3, coincides with the rest of the analyses, the relative density of the sample cannot explain the problem. The issue may be a consequence of the packing method, but this alone is probably not the entire solution.

However, in reality force chains are expected to carry the load, making a lot of particles not really involved (Majmudar and Behringer, 2005). Due to gravity, these grains will drop, creating small contacts with other grains. Still, the effect of gravity is assumed to be of minor importance to the measured response. Hence, it is possible that the number of rattlers is accurate compared to what would be expected in reality.

Undefined Rotations

By investigating the rotations measured for every grain at the end of the triaxial shearing, it is observed that DEM7 and DEM11 have three and four grains respectively that rotate uncontrolled. This is observed as "NaN (Not a number)" in the rotation output file. The issue, which is assumed to be numerically caused, seems to occur when loosely packed samples are compressed to high pressures ($1000 kPa$).

A possible explanation for the undefined rotations of certain grains is low inertia due to low mass. To investigate whether this explanation yields, the respective grain identities were studied. It was detected that out of the seven undefined values, three grains had the same identity. This identity represents the grain, out of the 78 in the library, with the lowest mass. It is therefore considered plausible that low grain mass could contribute in numerical issues when considering rotations, because they may rotate uncontrolled due to low inertia. However, three out of the four remaining grains with undefined rotation, have higher masses than the average grain mass. Therefore, low inertia of grains with low mass can only be part of the explanation to this matter.

The Effect of Time Step Size

The LS-DEM code enables adjusting the size of the time step, Δt. Our main analyses were conducted using Δt given as in Equation (7.3).

$$\Delta t = 0.2 \cdot \left(2 \sqrt{\frac{0.4 \cdot V_{min} \cdot \rho}{k_n}} \right) \tag{7.3}$$

Here, V_{min} refers to the volume of the smallest grain and ρ the grain density.

As mentioned in Section 3.1.3, LS-DEM uses an explicit time integration scheme, and requires sufficiently small time steps to ensure that the assumption of constant velocities and accelerations in each calculation step holds. When post processing the simulations, instabilities in the results were detected as significant leaps in the principal stresses after the 2% first time steps (visualized in Figure 7.3 (a)). In addition, several other leaps were detected during the shearing phase, easily seen for $p = 500\ kPa$ and $p = 1000\ kPa$ in Figure 5.3. This indicates numerical instabilities and was considered as something that should be further investigated.

To investigate this matter, the initial phase of the analyses was run several times, varying only the size of the time step and the amount of time steps in order to single out the effect of this on the stability of the solution. Based on these results, it is concluded that the default time step, as given in Equation (7.3), is not sufficiently small to capture the development of deviatoric stresses in the initial phase.

However, these analyses also showed that even though a higher time step leads to numerical instabilities in the initial phase, the calculated stresses after the initial phase coincided for all three investigated time steps sizes. In addition, the strains developed evenly and ostensibly independent of the time step size. These observations substantiates the accuracy of the obtained numerical results outside the initial phase, especially when going to large strains and approaching critical state. Still, initial values such as the initial shear stiffness, G_0, should be calibrated using a smaller time step.
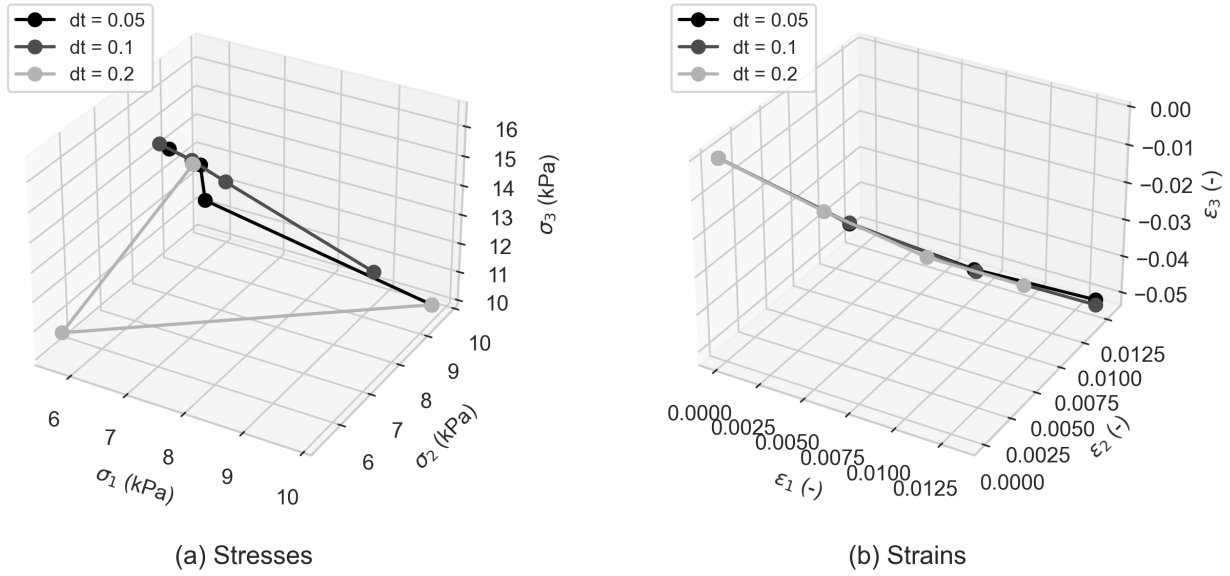
(a) Stresses   (b) Strains

Figure 7.3: Effect of time step size.

7.4   Contact Formulation

The existing version of LS-DEM calculates interparticle forces based on a linear contact formulation. This is inconsistent with reality, where the contact is considered non-linear. However, it is assumed that the effect of this simplification is insignificant when considering large strains. In addition, a more complex contact formulation would require additional input-parameters, which will make the physical parameter calibration process more complex and expensive. This may weaken the appealing simplicity of DEM. In addition, it will likely lead to higher computational costs.

As stated in Section 7.1, the initial shear stiffness, G_0, was calculated to be significantly lower than corresponding values documented in literature for Hostun sand. In LS-DEM, the linear contact model is implemented as a stress independent spring stiffness, and such a formulation may yield too low stiffnesses compared to experimental values for small deformations. It may therefore be assumed that the k_n-value applied in the simulations is too low for the calibration of G_0.

Stiffness of Particles

The stiffness level of the particles with linear-spring contact was calculated according to Equation (7.4).

$$\kappa = \frac{k_n}{p(\overline{d}_{eq})^{D-2}}$$

(7.4)

Where $\overline{d}_{eq}$ is the average equivalent grain diameter, k_n the normal stiffness in grain-to-grain contact and $D = 3$ the dimension of the system. The radius of the grains range between 5 and 20 pixels, and an average diameter of $\overline{d}_{eq} = 25\,pix = 0.37\,mm$ was used in these calculations. The respective κ's are summarized in Table 7.2.

Table 7.2: Stiffness level of the particles

Pressure, p (Pa)	κ (-)
10 000	8158
100 000	815.8
500 000	163.2
1 000 000	81.58

In practice for rigid particles, the overlaps are classified as small and thereby insignificant whenever $\kappa > 1000$ ("Advanced virtual course on Modeling Granular Processes for Energy and Environment (GPE) - Sciencesconf.org", 2021). Based on these results the particle overlaps are categorized as significant for the analyses with mean pressure, $p \geq 100 kPa$. However, in this thesis a linear contact model is used for the particle interaction and the presented requirement is therefore not completely applicable. In addition, the stiffness level criterion was found in a somewhat unofficial source (a video lecture series on granular materials). Anyway, the matter was investigated further by evaluating the effect of particle overlap.

Particle Overlap

The effect of particle overlap on the deformations measured at the boundaries was investigated in the isotropic compression phase for $p = 1000 kPa$. Since the calculation of void ratio assumes constant grain volume, volumetric strains calculated from void ratio (7.5) was compared with volumetric strains obtained from movement of the boundaries (7.6). Significant deviation between these would indicate considerable macroscopic volume reduction due to overlapping grains.

$$\varepsilon_V = \frac{e - e_0}{e_0 + 1} \tag{7.5}$$

$$\varepsilon_V = (1 + \varepsilon_1)(1 + \varepsilon_2)(1 + \varepsilon_3) - 1 \tag{7.6}$$

The effect of overlap was most prominent for the loosest packed sample, $e_0 = 1.0$. As visualized in Figure 7.4, the investigation showed no significant influence of particle overlap on the macroscopically measured volumetric strains. The same insignificant effect was also observed for the triaxial phase.

7.5 Computational Time

The simulations were run on a cluster with 32 CPUs. In order to reach critical state, simulating 4 000 000 - 5 000 000 time steps in the triaxial phase was necessary. This involved, for each calculation, a computational time of 80-90 hours. In addition, both packing of the sample and the isotropic compression phase needed to be simulated, both calculations running for approximately 24 hours. Consequently, one triaxial simulation with all its phases requires computational power for 5-6 days. Clearly, a significant amount of time has been spent in order to obtain the data presented in this thesis. However, the erroneous density used in this study may have had significant effect on the computational time. It will be less
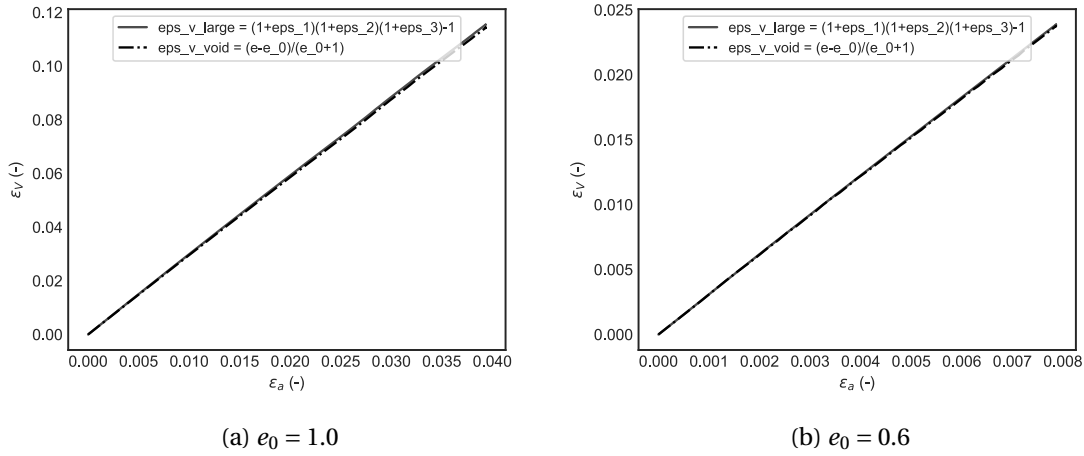
(a) $e_0 = 1.0$ (b) $e_0 = 0.6$

Figure 7.4: The effect of particle overlap for $p = 1000 \, kPa$. Only $e_0 = 0.6$ and 1.0 are visualized here, but the inital state $e_0 = 0.8$ yields similar results.

time consuming to run the simulation with a larger ρ.

Further, LS-DEM, compared to traditional DEM, offers greater flexibility in terms of enabling the modeling of grain shape. Thereby, it also comes along with greater computational costs, both when considering its RAM footprint but also in its evaluation time. Duriez and Bonelli (2021) state that LS-DEM requires 100 or 1000 times more megabytes of RAM than what is needed for a DEM simulation with spheres. In addition, considering evaluation time, they conclude that LS-DEM execution takes 25-300 times longer than classical DEM. These numbers certainly depend on the hardware and on the specific code implementation used. Accordingly, the statements need to be interpreted thereafter, but they certainly yield useful orders of magnitude when considering the computational efficiency aspect of LS-DEM.

The time and energy necessary to run each analysis is considered a major drawback to the method.

Chapter 8

Summary and Recommendations for Further Work

8.1 Summary and Conclusions

Chapter 2-3 gives a brief summary of the theoretical framework on which the SANISAND constitutive model and DEM are built. Section 3.3 presents the physical tests necessary to calibrate the DEM input parameters.

In Chapter 5 the calibration of a set of SANISAND input parameters by the use of LS-DEM simulations is presented. The calibrated critical stress ratio gave a good fit to all simulated analyses, and hence can be considered unique for the investigated material.

The calibrated SANISAND critical state line gave a better fit to the observed critical void ratios than often seen in experimental calibrations. However, between $p = 10\,kPa$ and $p = 500\,kPa$, the critical void ratio is approximately constant, before it does a negative leap at $p = 1000\,kPa$. This was not possible to capture with the SANISAND equation. Hence, it can not be determined whether the calibrated CSL is unique for the investigated material or not. This also yields for the phase transformation line, which was expected to be better defined for different initial states. The bounding surface, however, shows a good fit with the two different simulated initial void ratios. The kinematic hardening parameters could not be uniquely defined, but are set to values that provide adequate matches with the LS-DEM simulation results.

Due to the limitations in the LS-DEM contact formulation, it was difficult to define a unique initial shear stiffness, G_0. The rest of the SANISAND input parameters were found with trial and error, and hence their uniqueness is highly dependent on the uniqueness of the aforementioned parameters. With these observations, it can not be guaranteed that the calibrated set of input parameters is unique for the given material.

However, the parameter set was able to replicate the soil behavior observed in an independent numerical simulation. Due to time limitations, only the monotonic compression parameters were calibrated. In addition, the results were not compared to experimentally obtained results.

To investigate to what extent realistic grain representations affect the critical state parameters, some LS-DEM analyses were run substituting the true grain shape formulation with one yielding spherical grains. As expected, the collection of spherical grains reached a lower critical void ratio and critical stress ratio than the simulated Hostun sand.

Several numerical instabilities were detected in the simulation results. These instabilities should be investigated further, as they may be of significance for the measured macroscopic response, and hence the interpreted characteristic soil behavior and calibrated parameters.

8.2   Recommendations for Further Work

The remaining input parameters for a complete SANISAND parameter set should be calibrated, this includes running simulations of cyclic triaxial tests and extension tests. In addition, for a more accurate calibration of the bounding surface and dilatancy constants, an additional initial void ratio on the dense side should be included in the calibration.

It should be investigated whether the unexpected behavior in terms of almost constant critical void ratio between $p = 10 \, kPa$ and $p = 500 \, kPa$ is due to an error in the LS-DEM simulations run in this thesis. The same yields for the uncertainty in the calibrated phase transformation line. Due to the significant uncertainty of this, the existence of a unique phase transformation line, as proposed in the SANISAND formulation, should also be investigated.

The calibrated kinematic hardening parameters are not well defined in this study. Especially the c_h-value needs more work to be determined. Advantageously, a shorter time step should be applied. Then, by investigating initial LS-DEM results and SANISAND response while material is hardening (until peak), the accuracy of these parameters could be improved. This should be done for several void ratios from dense side. Generally, in existing research the calibration of c_h appears to be limitly investigated. Whether a unique value of this parameter actually exists, needs to be investigated.

For LS-DEM to be developed to the level where it routinely can substitute physical laboratory testing, a great amount of research remains to be done. It is especially crucial to validate the results from LS-DEM simulations by verifying that they coincide with corresponding laboratory investigations. The calibration done in this thesis could be verified by creating a digital twin of a sample of Hostun sand in the lab. This sample should be tested experimentally and numerically with LS-DEM. If the numerical and experimental results coincide with SANISAND simulations with this study's calibrated input parameters, the calibration can be considered credible. Such a validation will also strengthen LS-DEM's position as a supplement to conventional laboratory tests. However, some deviation must be expected, since the numerical simulations run in this thesis are impossible to replicate in the lab due to physical boundary conditions.

Since the sample preparation method affects the fabric of a sample, it should be investigated to what extent different configuration methods affect the final results. To do so, different preparation methods, like the ones used in the lab, should be incorporated in the code. Thereafter, it could be investigated whether an initial anisotropy in the sample affects the critical state parameters. And if so, to what extent.

The high number of rattlers in our investigated sample is also a matter that should be investigated further. It is possible that the limited share of active grain volume, results in interpreted soil parameters not representative for Hostun sand. However, the share of active grains may also be enough to realistically replicate the active force chains carrying the load in experimental results.

Further, our results may depend on the specific selection of grains constituting the sample. The extent of this dependency should be investigated. It should be verified that coinciding results are obtained with another selection of grains. The same analyses could also be performed on bigger samples with more grains, making the sample less sensitive to the specific grain selection.

Another motivation to run the simulations on a sample containing more than 16^3 grains, is to investigate whether there is a significant impact of the boundary conditions on the stiffness parameters. One type of sand should have consistent stiffness parameters. As the amount of grains in the sample increases, the share of grains in contact with the boundaries decreases. By sufficiently increasing the sample size, the impact from the boundaries diminishes and then the obtained results can be considered more reliable.

It is assumed that the linear contact formulation used in this version of LS-DEM is sufficient in terms of predicting a soil's response to large deformation. However, the formulation falls short when considering small deformations. This is a matter that should be further investigated. Increasing the k_n-value may contribute in recreating a more reliable initial elastic response of the soil. However, it needs to be noted that increasing the contact stiffness demands for greater computational power in terms of increased calculation time. Another option could be to incorporate a more accurate non-linear contact model in the code. Still, this will also lead to higher computational costs, in addition to a more comprehensive calibration process. Further, the current version of LS-DEM does not consider crushing of grains, a matter that should also, advantageously, be incorporated in the model. This is especially important when the granular material is exposed to large pressures.

LS-DEM can be used to collect a wide range of high quality sand behavior data, which does not exist today. By establishing extensive databases, one could accelerate the implementation of Machine Learning (ML) based techniques to calibrate constitutive sand models. Such methods requires a wide range of data, which is difficult to obtain by conventional laboratory testing.

Bibliography

Advanced virtual course on Modeling Granular Processes for Energy and Environment (GPE) - Sciencesconf.org. (2021). Retrieved 06/06/2021, from https://gpe.sciencesconf.org/

Bishop, A. W., & Henkel, D. J. (1962). *The measurement of soil properties in the triaxial test* [OCLC: 6439770]. E. Arnold.

Casagrande, A. (1979). *Liquefaction and cyclic deformation of sands : A critical review*. Harvard University, 1979, c1976. Retrieved 02/24/2021, from https://search.library.wisc.edu/catalog/999772343302121 Includes bibliographical references (pages 26-27).

Chian, S., Tokimatsu, K., & Madabhushi, G. (2014). Soil Liquefaction–Induced Uplift of Underground Structures: Physical and Numerical Modeling. *Journal of Geotechnical and Geoenvironmental Engineering, 140*, 04014057. https://doi.org/10.1061/(ASCE)GT.1943-5606.0001159

Cundall, P., & Strack, O. (1979). A discrete numerical model for granular assemblies. *Géotechnique, 29*(1), 47–65. https://doi.org/10.1680/geot.1979.29.1.47

Dafalias, Y. F. (1986). Bounding Surface Plasticity. I: Mathematical Foundation and Hypoplasticity. *Journal of Engineering Mechanics, 112*(9), 966–987. https://doi.org/10.1061/(ASCE)0733-9399(1986)112:9(966)

Dafalias, Y. F., & Manzari, M. T. (2004). Simple Plasticity Sand Model Accounting for Fabric Change Effects. *Journal of Engineering Mechanics, 130*(6), 622–634. https://doi.org/10.1061/(ASCE)0733-9399(2004)130:6(622)

Donze, F., Richefeu, V., & Magnier, S.-A. (2009). Advances in discrete element method applied to soil, rock and concrete mechanics. *Electronic Journal of Geotechnical Engineering, 8*.

Duran, J. (2000). *Sands, Powders, and Grains: An Introduction to the Physics of Granular Materials*. Springer-Verlag. https://doi.org/10.1007/978-1-4612-0499-2

Duriez, J., & Bonelli, S. (2021). Precision and computational costs of Level Set-Discrete Element Method (LS-DEM) with respect to DEM. *Computers and Geotechnics, 134*, 104033. https://doi.org/10.1016/j.compgeo.2021.104033

Fu, P., & Dafalias, Y. F. (2011). Study of anisotropic shear strength of granular materials using DEM simulation [_eprint: https://onlinelibrary.wiley.com/doi/pdf/10.1002/nag.945]. *International Journal for Numerical and Analytical Methods in Geomechanics, 35*(10), 1098–1126. https://doi.org/https://doi.org/10.1002/nag.945

Gao, H., & Chae, O. (2008). Touching tooth segmentation from CT image sequences using coupled level set method. *2008 5th International Conference on Visual Information Engineering (VIE 2008)*, 382–387. https://doi.org/10.1049/cp:20080343

Garcia, X., Latham, J.-P., Xiang, J., & Harrison, J. (2009). A clustered overlapping sphere algorithm to represent real particles in discrete element modelling [Publisher: ICE Publishing]. *Géotechnique*, *59*(9), 779–784. https://doi.org/10.1680/geot.8.T.037

Geden, O., & Schenuit, F. (2019). Climate Neutrality as Long-term Strategy: The EU's Net Zero Target and Its Consequences for Member States. https://doi.org/10.18449/2019C33

Irgens, F. (2008). *Continuum Mechanics*. Springer Science & Business Media.

Jostad, H. P., Dahl, B. M., Page, A., Sivasithamparam, N., & Sturm, H. (2020). Evaluation of soil models for improved design of offshore wind turbine foundations in dense sand [Publisher: ICE Publishing]. *Géotechnique*, *70*(8), 682–699. https://doi.org/10.1680/jgeot.19.TI.034

Jostad, H. P., Khoa, H. D. V., Karapiperis, K., & Andrade, J. (2021). Can LS-DEM be Used to Simulate Cyclic Behavior of Sand? [Conference Name: 16th International Conference on International Conference on Computer Methods and Advances in Geomechanics (IACMAG) ISSN: 2366-2557 Issue: 125 Meeting Name: 16th International Conference on International Conference on Computer Methods and Advances in Geomechanics (IACMAG) Number: 125]. In M. Barla, A. Di Donna, & D. Sterpi (Eds.), *Challenges and Innovations in Geomechanics* (pp. 228–235). Springer International Publishing. Retrieved 05/28/2021, from https://resolver.caltech.edu/CaltechAUTHORS:20210122-142125937

Karapiperis, K., Harmon, J., Andò, E., Viggiani, G., & Andrade, J. E. (2020). Investigating the incremental behavior of granular materials with the level-set discrete element method. *Journal of the Mechanics and Physics of Solids*, *144*, 104103. https://doi.org/10.1016/j.jmps.2020.104103

Kawamoto, R., Andò, E., Viggiani, G., & Andrade, J. E. (2016). Level set discrete element method for three-dimensional computations with triaxial case study. *Journal of the Mechanics and Physics of Solids*, *91*, 1–13. https://doi.org/10.1016/j.jmps.2016.02.021

Kawamoto, R., Andò, E., Viggiani, G., & Andrade, J. E. (2018). All you need is shape: Predicting shear banding in sand with LS-DEM. *Journal of the Mechanics and Physics of Solids*, *111*, 375–392. https://doi.org/10.1016/j.jmps.2017.10.003

Lam, W.-K., & Tatsuoka, F. (1988). Effects of Initial Anisotropic Fabric and 2 On Strength and Deformation Characteristics of Sand. *Soils and Foundations*, *28*(1), 89–106. https://doi.org/10.3208/sandf1972.28.89

Li, C., Xu, C., Gui, C., & Fox, M. D. (2010). Distance Regularized Level Set Evolution and Its Application to Image Segmentation [Conference Name: IEEE Transactions on Image Processing]. *IEEE Transactions on Image Processing*, *19*(12), 3243–3254. https://doi.org/10.1109/TIP.2010.2069690

Li, X. S., & Dafalias, Y. F. (2000). Dilatancy for cohesionless soils [Publisher: ICE Publishing]. *Géotechnique*, *50*(4), 449–460. https://doi.org/10.1680/geot.2000.50.4.449

Li, X. S., & Dafalias, Y. F. (2012). Anisotropic Critical State Theory: Role of Fabric [Publisher: American Society of Civil Engineers]. *Journal of Engineering Mechanics, 138*(3), 263–275. https://doi.org/10.1061/(ASCE)EM.1943-7889.0000324

Li, X. S., & Wang, Y. (1998). Linear Representation of Steady-State Line for Sand. *Journal of Geotechnical and Geoenvironmental Engineering, 124*(12), 1215–1217. https://doi.org/10.1061/(ASCE)1090-0241(1998)124:12(1215)

Lim, K.-W., & Andrade, J. E. (2014). Granular element method for three-dimensional discrete element calculations [_eprint: https://onlinelibrary.wiley.com/doi/pdf/10.1002/nag.2203]. *International Journal for Numerical and Analytical Methods in Geomechanics, 38*(2), 167–188. https://doi.org/https://doi.org/10.1002/nag.2203

Liu, H. Y., Abell, J. A., Diambra, A., & Pisanò, F. (2018). Modelling the cyclic ratcheting of sands through memory-enhanced bounding surface plasticity [Publisher: ICE Publishing]. *Géotechnique, 69*(9), 783–800. https://doi.org/10.1680/jgeot.17.P.307

Majmudar, T. S., & Behringer, R. P. (2005). Contact force measurements and stress-induced anisotropy in granular materials [Number: 7045 Publisher: Nature Publishing Group]. *Nature, 435*(7045), 1079–1082. https://doi.org/10.1038/nature03805

Meng, L., Lu, P., & Li, S. (2014). Packing properties of binary mixtures in disordered sphere systems. *Particuology, 16.* https://doi.org/10.1016/j.partic.2014.02.010

Nardelli, V., & Coop, M. R. (2018). The experimental contact behaviour of natural sands: Normal and tangential loading [Publisher: ICE Publishing]. *Géotechnique, 69*(8), 672–686. https://doi.org/10.1680/jgeot.17.P.167
Physical DEM input-parameters

Nordal, S. (2020). *Geotechnical Engineering Advanced Course, Lecture Notes.* Norwegian University of Science; Technology.

Papadimitriou, A. G., Bouckovalas, G. D., & Dafalias, Y. F. (2001). Plasticity Model for Sand under Small and Large Cyclic Strains [Publisher: American Society of Civil Engineers]. *Journal of Geotechnical and Geoenvironmental Engineering, 127*(11), 973–983. https://doi.org/10.1061/(ASCE)1090-0241(2001)127:11(973)

Petalas, A. L., Dafalias, Y. F., & Papadimitriou, A. G. (2019). SANISAND-FN: An evolving fabric-based sand model accounting for stress principal axes rotation [_eprint: https://onlinelibrary.wiley.com/doi/pdf/10.1002/nag. *International Journal for Numerical and Analytical Methods in Geomechanics, 43*(1), 97–123. https://doi.org/https://doi.org/10.1002/nag.2855

Raghunandan, M., Juneja, A., & Hsiung, B.-C. (2012). Preparation of reconstituted sand samples in the laboratory. *International Journal of Geotechnical Engineering, 6*, 125–131. https://doi.org/10.3328/IJGE.2012.06.01.125-131

Rothenburg, L., & Bathurst, R. J. (1991). Numerical simulation of idealized granular assemblies with plane elliptical particles. *Computers and Geotechnics, 11*(4), 315–329. https://doi.org/10.1016/0266-352X(91)90015-8

Salecon, J. (1974). *Application of the Theory of Plasticity in Soil Mechanics.*

Salvatore, E., Andò, E., Modoni, G., & Viggiani, G. (2018). *The Effects of Strain Localization on the Determination of Critical State Seen with Experimental and Numerical Models* [Journal Abbreviation: Trends in Mathematics Publication Title: Trends in Mathematics]. https://doi.org/10.1007/978-3-319-99474-1_30

Salvatore, E., Modoni, G., Andò, E., Albano, M., & Viggiani, G. (2017). Determination of the critical state of granular materials with triaxial tests. *Soils and Foundations -Tokyo-, 57*. https://doi.org/10.1016/j.sandf.2017.08.005

Schofield, A., & Wroth, C. (1968). *Critical State Soil Mechanics*.

Taiebat, M. T., & Dafalias, Y. F. (2008). SANISAND: Simple anisotropic sand plasticity model [_eprint: https://onlinelibrary.wiley.com/doi/pdf/10.1002/nag.651]. *International Journal for Numerical and Analytical Methods in Geomechanics, 32*(8), 915–948. https://doi.org/https://doi.org/10.1002/nag.651

Thornton, C. (2000). Numerical simulations of deviatoric shear deformation of granular media [Publisher: ICE Publishing]. *Géotechnique, 50*(1), 43–53. https://doi.org/10.1680/geot.2000.50.1.43

Triaxial Testing - an Introduction. (2017). Retrieved 05/14/2021, from https://www.vjtech.co.uk/blog/triaxial-testing-an-introduction

Vlahinić, I., Andò, E., Viggiani, G., & Andrade, J. E. (2014). Towards a more accurate characterization of granular media: Extracting quantitative descriptors from tomographic images. *Granular Matter, 16*(1), 9–21. https://doi.org/10.1007/s10035-013-0460-6

Wang, R., Fu, P., Zhang, J.-M., & Dafalias, Y. F. (2017). Evolution of Various Fabric Tensors for Granular Media toward the Critical State. *Journal of Engineering Mechanics, 143*(10), 04017117. https://doi.org/10.1061/(ASCE)EM.1943-7889.0001342

Wood, D. M. (1991). *Soil Behaviour and Critical State Soil Mechanics*. Cambridge University Press. https://doi.org/10.1017/CBO9781139878272

Yan, B., Regueiro, R. A., & Sture, S. (2010). Three-dimensional ellipsoidal discrete element modeling of granular materials and its coupling with finite element facets [Publisher: Emerald Group Publishing Limited]. *Engineering Computations, 27*(4), 519–550. https://doi.org/10.1108/02644401011044603

Yang, J., & Luo, X. D. (2015). Exploring the relationship between critical state and particle shape for granular materials. *Journal of the Mechanics and Physics of Solids, 84*, 196–213. https://doi.org/10.1016/j.jmps.2015.08.001

Yang, W., Zhou, Z., Pinson, D., & Yu, A. (2014). Periodic Boundary Conditions for Discrete Element Method Simulation of Particle Flow in Cylindrical Vessels [Publisher: American Chemical Society]. *Industrial & Engineering Chemistry Research, 53*(19), 8245–8256. https://doi.org/10.1021/ie404158e

Yu, H.-S. (2006). Multi-Surface and Bounding Surface Plasticity. *Plasticity and Geotechnics* (pp. 153–196). Springer US. https://doi.org/10.1007/978-0-387-33599-5_7

Zhao, C., Pinzón, G., Wiebicke, M., Andò, E., Kruyt, N., & Viggiani, G. (2021). Evolution of fabric anisotropy of granular soils: X-ray tomography measurements and theoretical modelling. *Computers and Geotechnics, 133*, 104046. https://doi.org/10.1016/j.compgeo.2021.104046

Appendix

Appendix A

Parameter Calibration

Python script for calibration of critical state line, bounding surface constant and dilatancy constant.

Calibration of CS parameters, SANISAND

```python
%matplotlib inline
import matplotlib.pyplot as plt
import numpy as np
from sklearn.linear_model import LinearRegression
plt.style.use('seaborn-darkgrid')
```

Critical State Line (CSL)

$\xi = 0.4$ was set before linear regression was used to locate the critical state line.

```python
#Load results from LS-DEM
############################

#Directories
logfile_path = r'C:/Users/odamo/Documents/LSDEM3D/LSDEM3D-Periodic/Output/logFiles/'
outDir = 'C:/Users/odamo/Documents/LSDEM3D/LSDEM3D-Periodic/Output/sample16/'

#Type of analysis
anType = 'triax'

#Initial conditions
init = ['VR1_p10',
        'VR1_p100',
        'VR1_p500',
        'VR1_p1000',
        'VR08_p10',
        'VR08_p100',
        'VR08_p500',
        'VR08_p1000',
        'VR06_p10',
        'VR06_p100',
        'VR06_p1000',
        'VR065_p100']

#Number of grains
nGrains = 16**3

#Scale stresses to kPa
scaleToKpa = 100/1.4741

#Define arrays to store the values
q_c = []
p_c = []
voidRatio = []
q=[]
p=[]
ec = []

#Import output for all analyses
for k in range (len (init)):
    outputDir = outDir + anType + '_' + init[k] + '/'
    incEps = np.loadtxt (outputDir + 'strain.dat')
    incSig = np.loadtxt (outputDir + 'stress.dat')
    incSig = incSig[:,:] * scaleToKpa

    incP = np.tile(np.sum(incSig, axis=1), (3,1)).T
    incP = 1/3 * (incP[:,0])
    incQ = incSig[:,2] - incSig[:,0]
```

```
    voidRatio.append (incEps[:,2])
    q.append (incQ)
    q_c.append (incQ[-1])
    p.append (incP)
    p_c.append (incP[-1])
    ec.append(incEps[:,2][-1])
```

In [8]:

```python
#CSL parameters:
alphac = 1.35
xi = 0.4
m = 0.01

#Perform linear regression to find the remaining critical state parameters
p_c = np.array(p_c)
p_eksp = (p_c/100)**xi
model_ec = LinearRegression().fit(p_eksp[0:-1].reshape((-1,1)), ec[0:-1])

#Critical state line parameters
lambda_c = - model_ec.coef_[0]
ec0 = model_ec.intercept_

print('lambda_c=', lambda_c)
print('ec0=', ec0)

#Sanisand equations
pc_cal = np.arange(1,1000,dtype=float) #array of cell pressures
qc_cal = alphac*pc_cal #q as a function of the cell pressures
ec_cal = ec0 - lambda_c * (pc_cal/100)**xi #critical state line


#Plotting
#q-p plot
fig, ax = plt.subplots(nrows=1, ncols=3, figsize=(16,5))
ax[0].plot(pc_cal,qc_cal, 'k', linestyle = '-.', label=r'$\alpha^c$=1.35')

for i in range (len(init)-1):
    ax[0].plot (p[i], q[i], label = init[i])

ax[0].plot(p_c, q_c, 'ko')
ax[0].legend(fontsize='9', loc='upper left')
ax[0].set_xlabel('p (kPa)')
ax[0].set_ylabel('q (kPa)')


#e-p plot
ax[1].plot(pc_cal,ec_cal, 'k', linestyle = '-.', label='CSL')

for j in range(len(init)-1):
    ax[1].plot(p[j], voidRatio[j], label = init[j])

ax[1].set_xlabel('p (kPa)')
ax[1].set_ylabel('e (-)')
#ax[1].legend(fontsize='9', loc='lower right')


#e-p logplot
ax[2].plot((pc_cal/100)**xi,ec_cal, 'k', linestyle = '-.', label='CSL')

for l in range (len(init)-1):
    ax[2].plot((p[l][0]/100)**xi, voidRatio[l][0], 'ko' )
    ax[2].plot((p[l][-1]/100)**xi, voidRatio[l][-1], 'k+')

ax[2].set_xlabel(r' $ \left( \frac{p}{100} \right)^{\xi} $')
ax[2].set_ylabel('e (-)')
ax[2].legend(fontsize='9', loc='upper left')

plt.show()
```
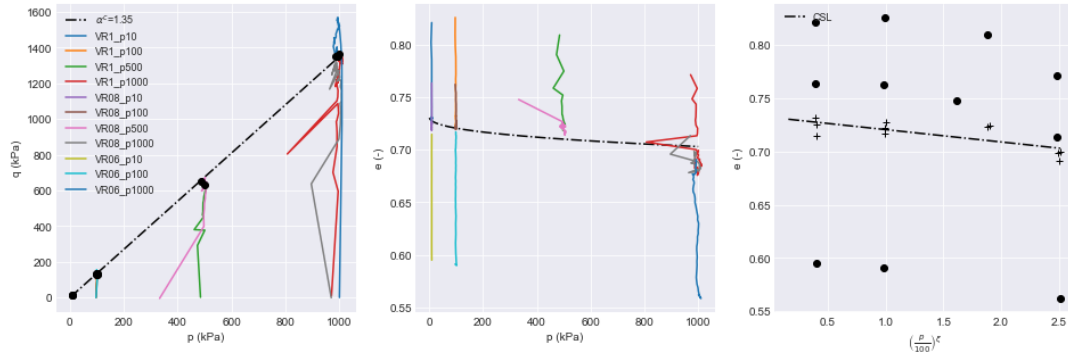
```
lambda_c= 0.011603763902106065
```

```
ec0= 0.7321304764439749
```


Bounding surface and phase transformation line

Determine the bounding surface constant, n^b, and the dilatancy surface constant, n^d.

For the phase transformation line, simulations of undrained tests (no volumetric strain) is used.

A good estimate of the value of n^d can be obtained by plotting the α^d/α^c versus the respective ψ^d of different tests. For $\psi = 0$, $\alpha^d/\alpha^c = 1$

Similar approach for n^b. Here, ψ^b and α^b are the the values of $\alpha\,(\eta)$ and ψ at peak stress-ratio state.

Peak stress ratio and the corresponding state parameters is found by plotting stress-ratio versus the state parameter.

Plotting α^c/α^b versus the respective ψ^b, an estimate of n^b can be obtained.

In [9]:

```python
#Calibration of nb
psi=[]

#Calculate the state parameters
for k in range (len(init)):
    incPsi = voidRatio[k] - ec0 + lambda_c*(p[k]/100)**xi
    psi.append(incPsi)


#Plotting stress ratio vs. state parameter. Extract the value from the dense analyzes.
fig, ax = plt.subplots(nrows=1, ncols=2, figsize=(16,5))
for k in range (len(init)):
    ax[0]. plot(psi[k], q[k]/p[k], label = init[k])
ax[0].set_xlabel(r'$\psi$ (-)')
ax[0].set_ylabel(r'$\eta$ (-)')

#Initial conditions, dense simulations
init_nb = ['VR06_p10',
        'VR06_p100',
        'VR06_p1000',
        'VR065_p100']
indDense = [8, 9, 10, 11]

#Extract the peak stress ratio and the corresponding state parameters
#The line should go through (0,0)
etas_nb = [0]
psis_nb = [0]

maxEta =[]

for k in range(len(init_nb)):
    incMaxEta = np.amax(q[indDense[k]]/p[indDense[k]])
```

```python
        maxEta.append(incMaxEta)
        array = np.where(q[indDense[k]]/p[indDense[k]] == np.amax(q[indDense[k]]/p[indDense[
k]]))
        index = array[0][0]
        etas_nb.append(np.log(alphac/incMaxEta))
        psis_nb.append(psi[indDense[k]][index])


    #Find the slope of the line by linear regression
    linPsi = np.linspace(-0.2,0.2,num=100)
    etas_nb = np.array(etas_nb)
    psis_nb = np.array(psis_nb)
    model_nb = LinearRegression().fit(psis_nb.reshape((-1,1)), etas_nb)
    regline_nb =  linPsi * model_nb.coef_[0]

    #Print the value given to nb
    print(r'n_b = ', model_nb.coef_[0])

    #Plot the obtained line in the mentioned space
    #ax2.plot(psi,fraction_b, 'k')
    ax[1].plot(linPsi, regline_nb, linestyle = '-.', label = r'$n^b=1.3$' )
    ax[1].plot(psis_nb, etas_nb, 'ko')
    ax[1].set_xlabel(r'$\psi$ (-)')
    ax[1].set_ylabel(r'$ln(\alpha^c/\alpha^b)$ (-)')
    ax[1].legend(fontsize='9', loc='upper left')


    #Plot the maximum values in the first graph
    ax[0].plot(psis_nb[1:], maxEta, 'ko')

    plt.show()
```
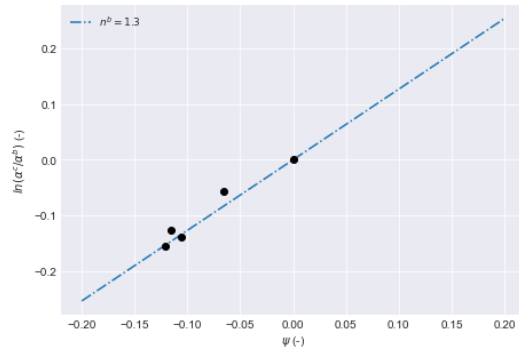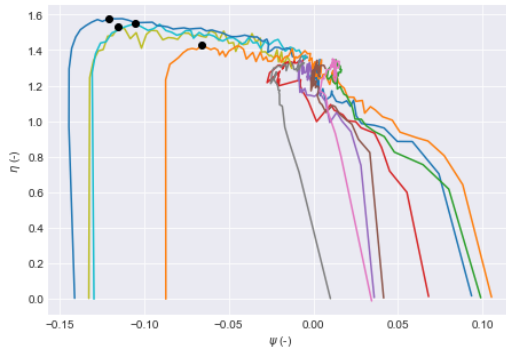
```
n_b =  1.267802285452294
```



```
In [10]:
```

```python
#Calibration of nd
#Import LS-DEM results from the undrained analyses
anType = anType = 'triax_undrained'
init_und = ['VR06_p10',
            'VR06_p100',
            'VR065_p100']

#Preallocate arrays to store extracted values
etas_nd = [0]
psis_nd = [0]

q_und = []
p_und = []
psi_und =[]
minp=[]
minq=[]

#Import the output for all analyses
for k in range (len (init_und)):
```

```python
        outputDir = outDir + anType + '_' + init_und[k] + '/'
        incEps = np.loadtxt (outputDir + 'strain.dat')
        incSig = np.loadtxt (outputDir + 'stress.dat')
        incSig = incSig[:,:] * scaleToKpa

        incP = np.tile(np.sum(incSig, axis=1), (3,1)).T
        incP = 1/3 * (incP[:,0])
        incQ = incSig[:,2] - incSig[:,0]

        voidRatio.append (incEps[:,2])
        q_und.append (incQ)
        p_und.append (incP)

        incPsi = incEps[:,2] - ec0 + lambda_c*(incP/100)**xi
        psi_und.append(incPsi)

        min_p = np.amin(incP)
        array = np.where(incP == np.amin(incP))
        index = array[0][0]
        min_q = q_und[k][index]
        minp.append(min_p)
        minq.append(min_q)

        etas_nd.append (np.log(((incQ[index])/(incP[index]))/alphac))
        psis_nd.append(incPsi[index])

#Find the slope of the line by linear regression
psis = np.linspace(-0.2,0.2,num=100)

#Can't force the regression line through 0 in Python, this was done i excel
nd_reg = 1.94
#nd equal to 2.0 is chosen for simplicity, due to the uncertainty
nd = 2.0
regLine = psis*nd_reg
dilLine = psis*nd

#Plot the obtained line
fig, ax = plt.subplots(nrows=1, ncols=2, figsize=(16,5))
for p in range(len(init_und)):
    ax[0].plot(p_und[p], q_und[p], label = init_und[p])
    ax[0].plot(minp, minq, 'ko')

    ax[1].plot(psis_nd, etas_nd, 'ko')

ax[1].plot(psis, dilLine, label = r'$n^d=2.0$')
ax[1].plot(psis, regLine, label = r'$n^d=1.94$')

ax[0].set_xlabel(r'$p$ ($kPa$)')
ax[0].set_ylabel(r'$q$ ($kPa$)')
ax[0].legend(fontsize='9', loc='upper left')
ax[1].legend(fontsize='9', loc='upper left')
ax[1].set_xlabel(r'$\psi$ (-)')
ax[1].set_ylabel(r'$ln(\alpha^d/\alpha^c)$ (-)')

plt.show()
```

```
In [ ]:
```